Lithosphere

Research Article

The Eureka Valley Landslide: Evidence of a Dual Failure Mechanism for a Long-Runout Landslide

Philip J. Shaller [iD], **Macan Doroudian, and Michael W. Hart**

ESi, 15235 Alton Parkway, Suite 120, Irvine, CA 92618, USA

Correspondence should be addressed to Philip J. Shaller; pjshaller@engsys.com

Long-runout landslides are well-known and notorious geologic hazards in many mountainous parts of the world. Commonly encompassing enormous volumes of debris, these rapid mass movements place populations at risk through both direct impacts and indirect hazards, such as downstream flooding. Despite their evident risks, the mechanics of these large-scale landslides remain both enigmatic and controversial. In this work, we illuminate the inner workings of one exceptionally well-exposed and well-preserved long-runout landslide of late Pleistocene age located in Eureka Valley, east-central California, Death Valley National Park. The landslide originated in the detachment of more than 5 million m^3 of Cambrian bedrock from a rugged northwest-facing outcrop in the northern Last Chance Range. Its relatively compact scale, well-preserved morphology, varied lithologic composition, and strategic dissection by erosional processes render it an exceptional laboratory for the study of the long-runout phenomenon in a dry environment. The landslide in Eureka Valley resembles, in miniature, morphologically similar "Blackhawk-like" landslides on Earth, Mars, and minor planet Ceres, including the well-known but much larger Blackhawk landslide of southern California. Like these other landslides, the landslide in Eureka Valley consists of a lobate, distally raised main lobe bounded by raised lateral levees. Like other terrestrial examples, it is principally composed of pervasively fractured, clast-supported breccia. Based on the geologic characteristics of the landslide and its inferred kinematics, a two-part emplacement mechanism is advanced: (1) a clast-breakage mechanism (cataclasis) active in the bedrock canyon areas and (2) sliding on a substrate of saturated sediments encountered and liquefied by the main lobe of the landslide as it exited the main source canyon. Mechanisms previously hypothesized to explain the high-speed runout and morphology of the landslide and its Blackhawk-like analogs are demonstrably inconsistent with the geology, geomorphology, and mineralogy of the subject deposit and its depositional environment.

1. Introduction

Long-runout landslides are notable geologic hazards in many mountainous regions of the world, including large portions of North and South America, Europe, and Asia. Risks include direct impacts to population centers and infrastructure by the highly mobile debris [1–3], downstream inundation hazards resulting from emplacement of debris into standing bodies of water [4], and the creation and failure of landslide dams [5]. In addition to the physical hazards represented by landslide dams, they also have the potential to impound large volumes of water in remote areas, affecting water quality and availabil-

ity in downstream areas [6]. We anticipate that these hazards will only increase over time in response to population pressures and infrastructure growth in and downstream from mountainous regions.

Despite these evident hazards, which cost the lives tens of thousands of individuals in the twentieth century alone, the mechanics of long-runout landslides remain enigmatic and controversial. The present work seeks to illuminate the inner workings of one exceptionally well-exposed and well-constrained long-runout landslide for application to the larger class of such features worldwide, with the joint goals of better constraining the hazards represented by these major

landslides and developing a better understanding of the role of environmental factors in promoting their long-runout behavior.

The Eureka Valley landslide lies immediately southeast of the Eureka Dunes at the southern end of the Eureka Valley, east-central California, Death Valley National Park, at latitude 37° 04′ 27″ N, longitude 117° 38′ 49″ W (Figure 1, Figure S1). The landslide originated from a rugged northwest-facing outcrop of Cambrian limestone and sedimentary strata in the central Last Chance Range in late Pleistocene time. We adopt the informal name Eureka Valley landslide (hereinaf-ter EVL) for the feature following McKeown and Bishop [7], who initially described it. Watkins [8] provided a mini-mum age estimate of 8.3-9.4 ka for the deposit based on Opti-cally Stimulated Luminescence methods and proposed a clay lubrication and/or subaqueous emplacement mechanism to explain its long-distance transport.

The EVL exhibits in relatively compact form numerous characteristic features of long-runout landslides in general and "Blackhawk-like" landslides in particular. Shaller [9] defined Blackhawk-like landslides as a subgroup of morpho-logically simple, dry rock long-runout landslides that resem-ble the well-known Blackhawk landslide of southern California [10]. Other terrestrial examples include the Silver Reef landslide of southern California [10], the New York Butte landslide in nearby Owens Valley, California [11], and a cluster of similar deposits documented in western Argentina [12]. Blackhawk-like landslides also occur on Mars [9] and dwarf planet Ceres (Figure 2).

We apply the term "long-runout landslide" herein in lieu of the terms "sturzstrom," "rock avalanche," and "rockslide avalanche," which are other frequently applied terms for such rapid, large-scale mass movements, to avoid the mechanistic associations implied by their usage. Also, avoided is the older term "megabreccia" from basin analysis, though these nota-ble sedimentary deposits frequently represent the remains of ancient long-runout landslide deposits.

Hsü [2] defined long-runout landslides as those having fall height (vertical distance from crown to toe, H) to travel length (horizontal distance between crown and toe, L) ratios of less than 0.6. Hsü [2] named this ratio the "fahrböschung" following Heim [16], which is literally translated from the original German as "travel slope." Heim [16] also referred to this measure as the "energy line."

A better understanding of the EVL is important for a vari-ety of reasons. Principally, the deposit provides valuable insights into the elusive transport mechanism(s) responsible for the long runout and other characteristics of rapid, large-scale landslides, a matter of considerable debate for over a cen-tury [17]. A better understanding of this fundamental geologic process is essential to improving landslide hazard risk assess-ments in mountainous terrain. Another valuable product of this study is a better understanding of the sedimentology of these deposits, which play a major role as petroleum reser-voirs in the Basin and Range region of the western United States [18, 19]. This study also provides new insights into the geology of the local area, including availability of surface water and the depth to groundwater during a recent glacial/-pluvial episode. Finally, an improved understanding of the

EVL and its morphological analogs has the reach goal of uti-lizing landslide morphology to remotely gage the past and present availability of liquid water on the surface of other planetary bodies, particularly Mars [9, 20].

2. Terminology

The EVL consists of three principal components (Figure 1): a prominent main lobe (hereinafter ML) located on the alluvial piedmont below the mountain front, a pair of "minor lobes" (irregularly shaped accumulations of limestone breccia) located on ridges and canyons southeast of the ML, and another pair of minor lobes located northwest of the ML run-out track. The ML itself consists of two principal compo-nents: a teardrop-shaped "distal heap" (hereinafter DH) and a raised lateral levee bounding the southern edge of its runout track. Based on comparison with morphologically similar landslides elsewhere (Figure 2), a similar levee is assumed to have originally bounded the northern side of the deposit that has since succumbed to erosion.

3. Setting

The EVL appears on the 1 : 62,500 scale Last Chance Quad-rangle geologic map of Wrucke and Corbett [13]. The deposit lies along the northwestern margin of the northeast-striking Last Chance Range, which exposes a layered sequence of Cambrian-age siltstone, sandstone, quartzite, and carbonate sedimentary strata (Figure 1). From oldest to youngest, these include the Early Cambrian Wood Canyon Formation, the Early to Middle Cambrian Zabriskie Quartzite, the Middle Cambrian Carrara Formation, and the Middle to Late Cam-brian Bonanza King Formation. Except where deformed along the range-bounding frontal fault, these deposits locally exhibit moderate southeasterly (into-slope) dips.

The range front is bounded by late Quaternary normal faults [21], including a pair of northeast-trending fault scarps that offset the landslide and adjacent alluvial surfaces. Profiles of the two normal fault scarps are consistent with M_w 7.1 to 7.3 events for the scarp-forming earthquakes [22]. The M_w 6.1 Big Pine earthquake, which struck near the western side of the valley on May 17, 1993, represents the largest historical seismic event recorded in Eureka Valley. This earthquake was associated with a series of small surface ruptures in the central part of the valley 6 to 21 km northwest of the landslide but no additional scarps in the vicinity of the landslide [14, 23].

In addition to seismic events of local origin, the Eureka Valley is subject to ground shaking from more distant earth-quake sources [23], including the Death Valley (13 km north-east) and Owens Valley Fault Zones (53 km southwest). The latter is associated with the 1872 Lone Pine earthquake, California's largest historical seismic event, estimated to have produced approximately level VIII ground shaking in the Eureka Valley [24].

The EVL is derived principally from bedrock of the Carrara and Bonanza King Formations. The Carrara For-mation locally consists of yellowish-brown, brown, and grayish-brown interbedded limestone, silty limestone, silt-stone, sandstone, and shale. The Bonanza King Formation
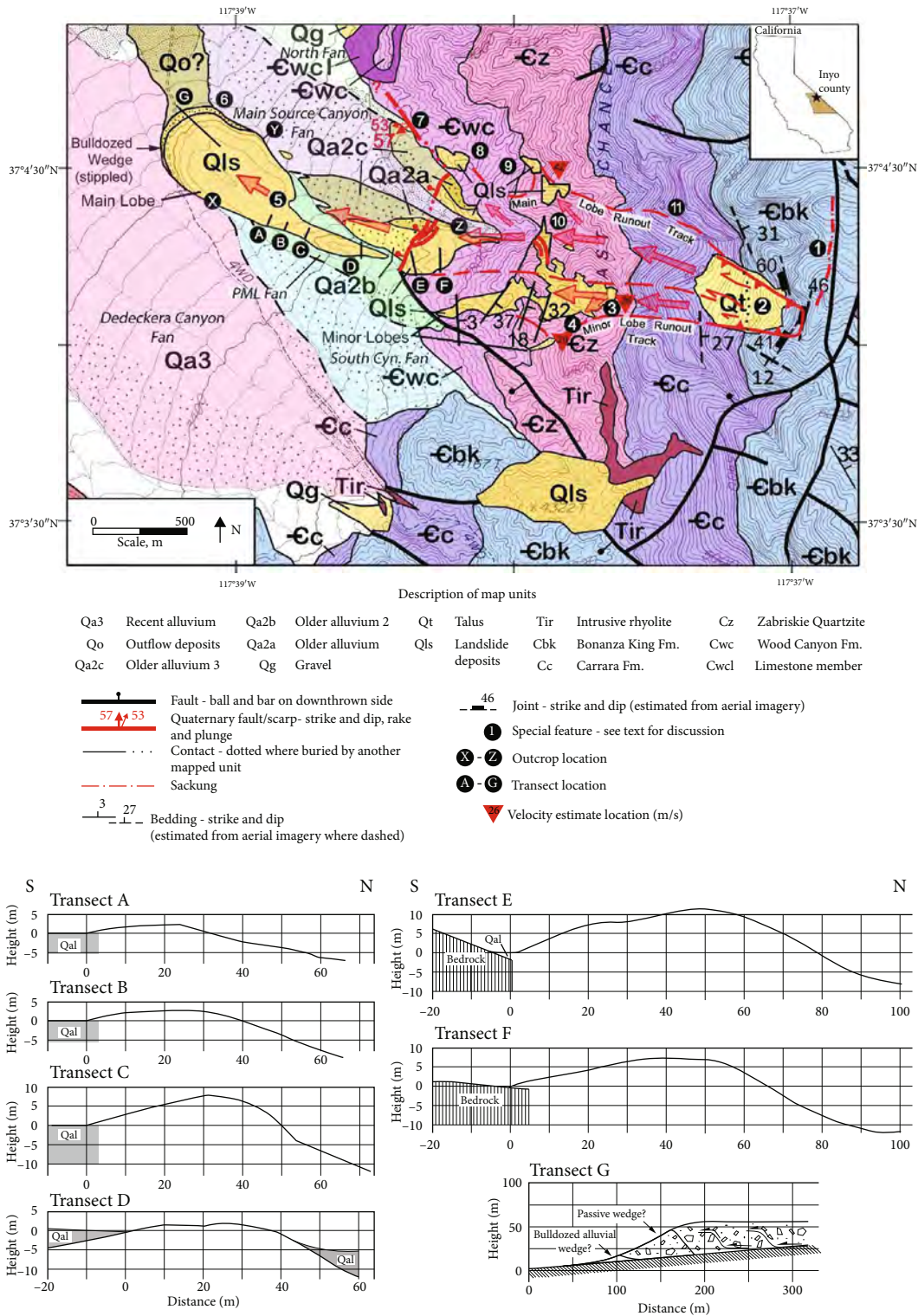
FIGURE 1: Geologic map of Eureka Valley landslide and vicinity, modified from Wrucke and Corbett [13] and Schlom and Knott [14]. Base map U.S. Geological Survey. Stippled areas on alluvial fans indicate inactive and/or minimally active surfaces.

consists of black dolomitic limestone with occasional bands of white limestone.

The EVL originated on a steep northwest-facing slope in the upper reaches of the unnamed "main source canyon" (hereinafter MSC), a 341 ha watershed exhibiting approxi-mately 1,040 m of vertical relief and a peak elevation of approximately 2,130 m. The unnamed adjacent southerly watershed contains the principal minor lobe (hereinafter PML). It is a 36 ha watershed with approximately 415 m of vertical relief and a peak elevation of about 1,550 m. Other
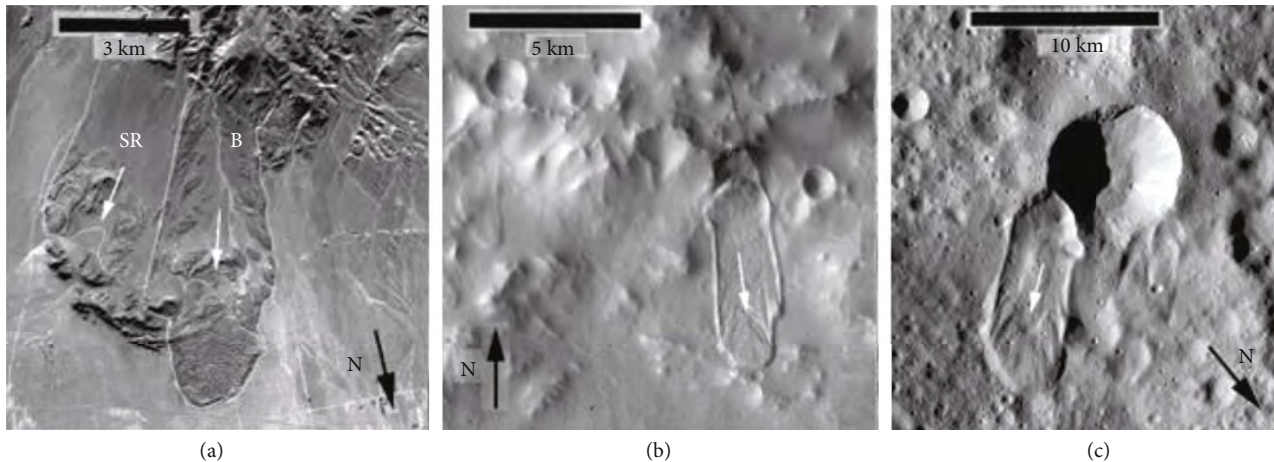
FIGURE 2: Examples of "Blackhawk-like" landslides on Earth, Mars, and Ceres (image sources: USGS, NASA). Maximum toe thickness ranges from 30 m at Silver Reef (SR) and Blackhawk (B) landslides ((a), outlined) to 80 m at Martian landslide located along the north rim of crater Montevallo (b) to approximately 130 m for unnamed Ceres landslide at (c), located at 50˚ N, 27˚E [15]. White arrows indicate travel direction.

nearby watersheds affect the EVL by way of their associated alluvial fans, which are labeled on Figure 1. Table 1 summarizes the key characteristics of these watersheds.

Schlom and Knott [14] mapped the EVL and nearby alluvial fan surfaces (Figure 1). Alluvium overlying the proximal portion of the landslide today stands as much as 25 m above the active channel draining the MSC. The alluvium has an exposed thickness of up to 6 m and locally exhibits a well-developed desert pavement, pitted carbonate clasts, and dark brown varnish on noncarbonate clasts. These characteristics resemble alluvial surfaces in nearby Death Valley dated to 60-80 ka [25].

The 25 m of fan head incision that followed deposition of the proximal alluvial fans represents, in part, a return to pre-disturbance watershed characteristics. Other geomorphic evidence in the vicinity suggests, however, that the incision observed at the mouth of the MSC includes the effects of tectonic- and/or climate-related processes unrelated to the landslide [26]. This evidence includes ~2 to 5 m of fan head erosion and ~1 to 2 m alluvial fan incision along nearby portions of the range front. The southerly margin of the ML is also experiencing active erosion, as are the margins of the dune-clad alluvial deposit to the northwest (Figure 1, unit Qo?). Potential underlying causes of this widespread erosional activity includes the declining activity of the range-bounding normal faults and/or a reduction in debris production associated with the shift from Pleistocene to Holocene climate conditions.

Other notable and relevant geologic features present in the vicinity of the EVL include (see Figure 1 for feature locations):

Feature 1: a ridgetop fissure (sackung) located above and to the north of the landslide source area

Feature 2: a large talus accumulation occupying the head-scarp bowl vacated by the landslide (Figure S2)

Feature 3: a small body of playa sediments located near the wind gap at the head of the PML (Figure S3)

Feature 4: an erosionally sculpted arch of landslide debris that exposes the base of the PML (Figure S4)

Feature 5: a small playa located along the upslope edge of the DH (Figure S5)

Feature 6: the eroded lateral margin of a possible outwash lobe mantled by drift sand and a veneer of rhyolite clasts derived from Dedeckera Canyon (Figure S6)

Feature 7: intermittent exposures of the main frontal fault with mullion structure, drag folding, and light-colored travertine deposits (Figure S7)

Feature 8: an isolated mass of Carrara and Bonanza King landslide breccia in preserved stratigraphic sequence with clastic dike and probable reworked travertine deposits (Figure S8)

Feature 9: a small lobe of Carrara limestone breccia that overtopped the northern edge of the source watershed at approximately elevation 1,295 m, corresponding with the westerly limit of an erosional trim line (Figure S9)

Feature 10: a series of locally reworked outcrops of Carrara limestone breccia that represent erosional remnants of a once extensive body of breccia deposited located near the mouth of the MSC (Figure S10)

Feature 11: an erosional "trim line" roughly 50-100 m above the canyon floor that apparently formed by scour from passing landslide debris; the trim line is visible in Google Earth imagery running about 700 m along the north side of the MSC

These features were field verified where feasible except for Features 1, 2, and 11, which were interpreted solely from Google Earth imagery and/or remote field observation.

4. Physical Characteristics of the EVL

Tables 2–5 summarize the key physical characteristics of the EVL. Except where noted, all elevations, distances, and area measurements rely on Google Earth topography. Many of the morphological and textural characteristics of the EVL resemble features exposed on other long-runout landslide deposits. Table 2 lists these features along with their relative prevalence elsewhere [9].

As noted, the EVL consists of the prominent main lobe and a series of minor lobes. The initial separation of the

TABLE 1: Watershed characteristics.

Name	Area (ha)	Max. relief (m)	Max. elevation (m)	Alluvial fan area (ha)
North canyon	71	650	1,670	24
Main source canyon (MSC)	341	1,040	2,130	107
Principal minor lobe (PML) canyon	36	415	1,550	16
South canyon (PML adjacent)	77	635	1,800	50
Dedeckera Canyon	3,500	1,225	2,350	303

TABLE 2: Key physical characteristics of the EVL.

Property	Occurrence	Present in EVL?
Distinct boundaries	Ever-present	✓
Brecciated rock mass	Ever-present	✓
Reverse grading	Common	✓
3D jigsaw puzzle blocks	Common	✓
Preserved headscarp stratigraphy	Common	✓
Incorporated substrate material	Common	✓
Raised distal rim	Rare	✓

TABLE 3: Key EVL geometric values—main lobe.

Property	Entire	Alluvial fan	Distal heap
Fall height, H (m)	935	167	42
Runout length, L (m)	3,530	1,700	680
Width (m)	400	400	400
Area (ha)	—	70	27
Thickness, max. (m)	32	32	32
Volume ($\times 10^6$ m^3)	4.7	4.7	4.3
Fahrböschung (H/L)	0.26	0.1	0.06
Tan (H/L) (degrees)	15	5.6	3.4

slidemass into distinct lobes occurred when the speeding mass encountered a bedrock ridge lying across its path in the upper reaches of the MSC. Roughly 60% of the debris passed to the right (north) of this ridge and traveled downhill to form the ML and the northerly minor lobes; the remaining 40% passed to the left (south), forming the PML and a small subsidiary lobe. The irregular shapes of the various minor lobes result from their originally sinuous travel paths combined with postemplacement erosion.

Debris that formed the ML remained channelized for the first ~1,500 m of its downhill run, emerging from the mouth of the MSC with a width of about 300 m and a thickness in excess of about 15 m, based on the geometry of the canyon and the height of the levee at its mouth (Figure 1, Profiles E and F). It thereafter experienced considerable spreading and thickening as it descended the alluvial fan below the mouth of the canyon. From an initial width of ~300 m, the ML expanded to a width of ~400 m by the conclusion of movement (i.e., a 133% increase) and experienced as much as 20 m of distal thickening.

The ML's distinctive south lateral levee, despite appearances, is not a simple constructional landform akin to a mud-flow levee. Rather, its inner edge typically averages about 10 m lower than its corresponding outer margin based on five Google Earth topographic profiles (Figure 1, Transects A-F), confirmed with field measurements of Transects A-C using a Ziplevel® electronic water level. These observations imply that the ML eroded its bed during emplacement, incorporating as much as 1.6 million m^3 of substrate material as it descended the alluvial fan (corresponding to 10 m of scour over the 16 ha area bounded by the levees, mountain front, and distal heap). This implied volume neatly balances the volume represented by the widening and thickening of the ML.

Table 5 summarizes the area and volume of the EVL and its major components, including the effects of alluvial scour and a bulking factor of 25% for the conversion of intact rock to breccia [27]. As indicated, the estimated total volume of intact limestone represented by the various lobes of the EVL ranges from 4.2 to 5.5 million m^3 depending on the extent of basal scour that accompanied emplacement of the ML.

4.1. Sedimentology

4.1.1. Main Lobe. The ML consists principally of clast-supported, angular to subrounded breccia (Figure S11) that exhibits crude reverse grading, as represented by numerous large isolated boulders that litter the surface of the deposit (Figure S12). Grain sizes vary widely, ranging from silt- or clay-sized rock flour up to boul-ders several meters in diameter. In several locations, the slide debris is pervasively fractured but minimally disarticulated (Figure S13), a texture referred to elsewhere as three-dimensional jigsaw puzzle breccia [10]. At a finer scale, crude color banding, often of subhorizontal orientation, is common. Abrupt grain size and other textural changes, the occasional appearance of gouge-like material, and the presence of contorted bedding adjacent suggest that these features represent internal shear zones (Figure S14). On the northern side of the DH (Figure 1, Location Y), one of these shear features steepens dramatically to an angle of 56° (dip to southeast, upslope) giving the appearance of reverse faulting (Figure S15).

At outcrop scale, the eroded southern edge of the ML offers a spectacular example of preserved headscarp stratigraphy (Figure S16). Here, the basal two-thirds of the exposure consists of brown to yellow-brown Carrara Formation breccia, the upper third of gray, white, and black Bonanza King Forma-tion breccia. The latter includes a distinctive, distended white marker bed, as well as most of the boulders that project above the surface of the deposit. These disarticulated bedrock units are radically attenuated relative to their intact geometry on the slope but otherwise preserve their original stratigraphic sequence and relative thicknesses

Table 4: Key EVL geometric values—minor lobes.

Property	Principal minor lobe	Lesser minor lobe (S)	Lesser minor lobe (N1)	Lesser minor lobe (N2)
Fall height, H (m)	530	335	695	660
Runout length, L (m)	1,615	1,070	1,715	1,950
Length below last drainage divide (m)	900	200	120	410
Width, max (m)	300	20	50	100
Area (ha)	11	0.05	0.5	1.4
Thickness, max. (m)	35	3	4	15
Thickness, avg. (m)	17	2	2	6
Volume ($\times 10^6$ m^3)	2	0.001	0.01	0.08
Fahrböschung (H/L)	0.33	0.31	0.41	0.34
Tan (H/L) (degrees)	18	17	22	19

Table 5: Key EVL geometric values—overall.

Property	Main lobe	Minor lobes	Total
Volume, bulked ($\times 10^6$ m^3)	4.7	2.1	6.8
Volume, scoured ($\times 10^6$ m^3)	0-1.6	0	0-1.6
Volume, limestone breccia ($\times 10^6$ m^3)	3.1-4.7	2.1	5.2-6.8
Volume, unbulked ($\times 10^6$ m^3)	2.5-3.8	1.7	4.2-5.5
Area (ha)	70	13	83

Table 6: Attenuation ratio for main lobe lateral exposure.

Layer	Thickness Slope (m)	Thickness Deposit (m)	Attenuation ratio
Gray	N.A.	N.A	N.A.
White	12	0.3	40 : 1
Black	104	2.6	40 : 1
Brown	73	1.8	41 : 1
Gray-brown	70	1.7	41 : 1
Yellow-brown	88	>1.5*	N.D.*

N.A.: not applicable; *N.D.: not determined. If the attenuation ratio is consistent, the base lies about 0.6 m below the base of the field exposure, and the deposit thickness is anticipated to be roughly 2 m.

with little intermixing. Comparison of color band thicknesses at Location X (Figure 1) with the intact correlative bands on the slope yields an attenuation ratio of approximately 40 : 1 for the displaced material (Table 6). Based on comparison with the bedrock relations exposed in the headscarp bowl, this attenuation ratio implies that the base of the landslide likely lies less than a meter below the base of the exposure.

The more extensively eroded northern side of the ML exposes a more complex array of textures and structures. Near the mouth of the MSC, the breccia overrides a bedrock ridge in the Wood Canyon Formation, then cuts obliquely across the original alluvial surface (Figure 1, Location Z). Outcrops in this area expose gray to white limestone breccia

overlying limestone-dominated alluvium containing a minor admixture of other rock types. Similarities in color and texture between the breccia and the underlying alluvium render these units comparatively difficult to distinguish in many field exposures, and much of the exposed material may represent comingled or interfingering deposits of the two materials [28]. Locally, however, the landslide-alluvium contact is readily identified. At one such location, the contact is marked by a 30 cm thick, matrix-supported, normally graded, silty sand with gravel interval (Figure S17). Larger gravel and cobbles appear to have settled to the bottom of this layer, and its upper sur-face interfingers with the overlying landslide breccia. Overall, the texture is suggestive of a fluidized boundary layer between the landslide and the alluvial substrate.

4.1.2. Principal (Southerly) Minor Lobe. Unlike the ML, the PML consists almost entirely of brown to yellow-brown Carrara limestone breccia. A veneer of gray limestone breccia caps many outcrops, however, suggesting another instance of preserved headscarp stratigraphy, with Bonanza King breccia overlying Carrara Formation-derived material. As in the ML, subhorizontal internal slip surfaces are common, often juxtaposing breccia of contrasting color and texture. Locally, bands of uniformly colored and textured breccia are deformed into arches and chevron folds with wavelengths and amplitudes ranging from roughly 2 to 10 m (Figure S18).

At one location at the base of an erosionally sculpted arch (Figure 1, Feature 4), an approximately 10 cm thick boundary layer lies sandwiched between intact bedrock below and breccia of contrasting texture and color above. This layer is com-posed mainly of poorly sorted sand- and gravel-sized limestone breccia (Table 7) and is traceable laterally to a point where it departs from the bedrock surface and intrudes into the overlying slidemass. The results of an XRD analysis of material collected from the boundary layer confirm the dominant carbonate lithology of the landslide and the extremely low concentration of clay minerals contained therein (Table 7).

Nearby, a local depression in the bedrock contains up to 30 cm of angular gravel and cobbles, which in turn is overlain by finer breccia. We interpret these relations to represent localized deposition from the coarse-grained leading edge

TABLE 7: Gradation and XRD test results on basal minor lobe sample.

Gradation	Size range (mm)	Weight percent	Material	Weight percent
Gravel	>5	48.4	Calcite	71
			Dolomite	21
Sand	0.075-5	36.9	Quartz	4
			K-feldspar	1
Fines	0.002-0.075	14.7	Plagioclase	1
			Pyrite	tr*
			Illite/smectite	tr*
			Illite/mica	2
2 microns	<0.002	2.0	Kaolinite	tr*
			Chlorite	tr*
			Total	100

Gradation analysis performed by Hushmand Associates, Inc. XRD analysis performed by Petricore. *tr = <0.5%.

of the landslide, which filled low spots in the topography as it descended the slope (Figure S19 and Figure S20). Similar relations exist at the base of the Martinez Mountain rock avalanche of southern California, where they are present at a much larger scale [9, 29].

Local exposures of the PML exhibit sufficient fines content to develop a matrix-supported texture. Small-scale levees occur along the margins of the deposit in this general area that resemble those commonly bounding mudflow deposits [30]. Despite the presence of these locally fluid-appearing textures and features, the dominant clast-supported texture of the landslide is quite distinct from a typical debris flow deposit.

4.1.3. Northerly Minor Lobes. Isolated masses of landslide breccia overtopped the northerly drainage divide near the mouth of the MSC and came to rest on the slopes of adjacent northerly canyons (Figure 1, Locations 8 and 9). At Location 8, a body of landslide breccia about 10 m thick drapes over the ridge dividing the watersheds. This exposure consists mainly of Carrara Formation breccia, capped by blocks of black Bonanza King limestone, representing a third example of preserved stratigraphic sequence in the landslide mass. Blocks of Carrara and Bonanza King limestone exposed near the summit of this side lobe exhibit three-dimensional jigsaw puzzle texture, as observed elsewhere on the landslide, along with cavernous weathering (Figure S21).

The base of the landslide is well exposed in the vicinity of Location 8 for tens of meters along its contact with the underlying Wood Canyon Formation. At this location, locally derived Wood Canyon clasts form a substantial admixture to the predominantly Carrara-derived landslide breccia, indicating substantial local scour of the bedrock surface (Figure S22). Nearby, a light brown to white matrix infiltrates the landslide breccia along the contact and extends into the body of the deposit. This pale colored matrix, unique among expo-sures of the landslide, suggests the probable local incorpora-tion of frontal fault-associated travertine deposits during runout. This material appears to have intruded the fractured surface of the underlying bedrock,

loosening and detaching angular slabs of rock via a stoping-type mechanism (Figure S23). Similar material can be observed nearby mixing into the body of the debris, as well as forming a clastic dike that intrudes a block of black Bonanza King limestone near the summit of the deposit, approximately 10 vertical meters above the base (Figure S24).

An isolated mass of Carrara Formation breccia occurs at Location 9, where it overtopped the drainage divide from the MSC and cascaded down a steep north-facing slope. The resulting deposit is a disorganized mass of gravel, cobbles, and boulders.

5. Discussion

5.1. Slope Preparation and Initiation. A series of factors set the stage for the EVL slope failure. Quaternary uplift along the Eureka Valley Fault Zone produced the requisite uplift and resulting steep relief along this portion of the mountain front, accompanied by differential weathering between the Carrara and Bonanza King Formations. As is common for these units in the Death Valley area, the siliceous Carrara limestone is a slope former, whereas the overlying Bonanza King limestone and dolomite is a cliff-forming unit [31]. On this basis, we hypothesize that a protracted period of preferential weathering of the Carrara Formation resulted in progressive erosional undercutting of the Bonanza King Formation in the source area of the EVL in advance of the slope failure.

Intersecting, valley-dipping, moderately to steeply inclined joint sets within the Bonanza King Formation further reduced the stability of the oversteepened slope. Based on Google Earth imagery, these joint sets appear to control the geometries of large planar slope areas above the talus accumulation in the source area. Figure 1 shows the estimated orientations of these joint sets, calculated by application of three-point geometry methods. The sheer slopes and active tectonic environment contributed to the formation of an apparent sackung feature on the ridgeline northeast of the headscarp bowl that projects towards the head of the landslide (Figure 1, Feature 1). Sackung features form in response to gravitational spreading of ridgelines due to a loss of lateral support (typically in glaciated terrains) or due to intermittent movement in response to seismic ground accelerations [32]. This observation suggests that some of the joint surfaces in the headscarp vicinity have experienced a protracted history of differential movements.

5.2. Failure Geometry and Volume. Comparison of the bedrock stratigraphy with the stratigraphy exposed in the ML indicates the highest portion of the scarp preserved in the final deposit is a prominent white limestone marker bed that outcrops at the edge of the talus-mantled headscarp bowl that is projected to lie at around elevation 1,737 m within the bowl. The slope length between the marker bed and base of the headscarp bowl at around elevation 1,545 m is approximately 386 m. Given that the headscarp bowl is approximately 300 m wide, we calculate that the portion of the slide block preserved in the final deposit originally measured approximately 300 m wide by 386 m long (parallel to slope)

TABLE 8: Upper headscarp volumes and geometries.

Slope section	Elevation (m) Lower	Elevation (m) Upper	Area (ha)	Average thickness (m)	Volume ($\times 10^6$ m^3)
Main scarp	1,545	1,737	10.7	35–47	4.1–5.4
Upper scarp	1,737	1,780	5	22–29	1.1–1.5
High scarp	1,780	1,900	1.7	10	0.17
Erosion valley	1,892	1,985	1.6	3	0.05
Talus slope	1,545	1,780	15	3.5	0.5

by 35 to 47 m thick (normal to slope). The lower thickness estimate corresponds to the case of maximum ML alluvial scour; the greater thickness applies to the nonscour case.

The geomorphology of the headscarp bowl implies that the original slope failure contained more material than is accounted for by the existing landslide deposits. This missing material consists of Bonanza King bedrock originally present in the slope area above the white marker bed, extending upslope to the crown of a fresh-appearing planar scarp at about 1,900 m. A distinct break in slope and color change marks the top of this scarp, which is located approximately 50 m below the ridge line; above this limit, the rock mass is darker and more heavily weathered. Some of the rock encompassed in the slope failure remained in the headscarp bowl to form the prominent talus deposit present therein, but the majority exited the headscarp and was presumably deposited in the MSC.

Table 8 provides the estimated elevations, dimensions, and volumes of rock displaced from the headscarp bowl during the EVL. It also provides an estimate of the volume of debris that still resides in the headscarp bowl as talus (approximately 0.5 million m^3). Postlandslide erosion of a steep-walled watershed at the head of the scarp produced roughly 0.05 million m^3 about one-tenth of this total. The remaining 0.45 million m^3 consists of material derived from the original slope failure that remained in the headscarp bowl after the failure. This accounting raises our estimate of the volume of the initial slope failure to between 4.9 and 6.6 million m^3 but yields a "missing" volume of approximately 0.8 to 1.2 million m^3 that is neither accounted for by the talus or by our current accounting of landslide debris. We evaluate the implications and disposition of this additional displaced material in the subsequent discussion.

5.3. *Triggering.* The triggering event for the landslide is unknown. The proximity of the EVL to active Quaternary faults makes a plausible, though controvertible, case for seismic triggering of the landslide. Rainfall in Eureka Valley is sparse, with rainfall totals between 2013 and 2019 averaging only 62 mm/yr. [33] Much of the annual precipitation today occurs during winter and likely falls as snow on the higher surrounding peaks. Even during late Pleistocene time, aver-

age yearly precipitation likely did not exceed twice the modern value [34, 35]. Because snow accumulation was likely significant at higher elevations in late Pleistocene time, frost wedging represents a potential additional contributing factor to the slope failure. Given the extremely steep topography in the source area, accumulation of direct rainfall or elevation of a groundwater table in the ridge both seem unlikely factors in triggering the landslide, but the steep terrain could contribute to slope creep (likely focused along on preexisting discontinuities), a phenomenon that has been known to accelerate into large-scale slope failure of this magnitude [9, 16].

5.4. *Post-EVL Landform Evolution.* The emplacement of the EVL affected runoff and sediment production from several contiguous watersheds along the range front (Figure 1, Table 1), which, in turn, modified the geomorphology of the landslide. These modifications have altered the deposit morphology sufficiently to require separate treatment of the evolution of the local watersheds and their associated alluvial fans. These relevant watersheds include:

(1) The MSC, in which the landslide originated

(2) The adjacent unnamed "north" watershed which hosts two minor debris lobes of landslide debris

(3) The adjacent unnamed watershed immediately south of the MSC that hosts the PML and whose alluvial fan (shaded green in Figure 1) abuts proximal sections of the main lobe's intact southerly levee

(4) The "south" watershed, located adjacent to the PML-hosting watershed and north of much larger Dedeckera Canyon. The alluvial fan associated with this small canyon (shaded blue in Figure 1) abuts and is actively eroding the central reach of the intact lateral levee

(5) The large Dedeckera Canyon watershed (shaded pink in Figure 1), whose associated alluvial fan abuts the toe and distal portions of the ML

Landslide debris composing the PML continues to choke the small watershed in which it came to rest. Presumably, similar bodies of landslide debris once occupied portions of the MSC that have since been flushed from the canyon by more vigorous fluvial activity in that larger and more elevated canyon, contributing to formation of the sequence of alluvial fans found at and below the mouth of the canyon (Figure 1).

Each of the five watersheds discussed above has experienced at least 2 to 5 m of late Quaternary incision at the mountain front, reflecting the effects of long-term tectonic and/or climatic processes. This incision has exposed the range-bounding normal fault and associated distinctive travertine deposits along the range front north of the ML (Figure 1, Feature 7). We interpret the much greater 25 m incision of the MSC to result from the additional short-term disturbance caused by emplacement of the EVL.

The alluvial fans associated with each of these canyons have also experienced at least 1 to 2 m of incision, resulting in the isolation of large, elevated, inactive, or minimally

active fan surfaces (Figure 1, stippled pattern). The active, incised portion of the Dedeckera Canyon fan intercepts the toe of the ML. It also contains distinctive rhyolitic volcanic debris, apparently a result of a recent incidence of stream piracy in the upper canyon that is actively eroding a large exposure of volcanic bedrock. Outcrops of volcanic rock are absent or much less prevalent in the other contiguous watersheds. As a result, alluvium associated with the active portion of the Dedeckera Canyon fan is distinguishable by its high concentration of these volcanic cobbles.

Following emplacement of the EVL, stream erosion flushed significant volumes of landslide debris from both the MSC and the canyon containing the PML, isolating a small body of lacustrine deposits at the head of the PML (Figure 1, Feature 3) and contributing to the construction of proximal alluvial fans at the mouths of both canyons. The fans constructed at the mouth of the MSC mantled most of the ML upstream from the DH (Figure 1).

Exposures near the mouth of the MSC indicate that the fans constructed there ranged up to a maximum of about 6 m in thickness. We estimate that these fans originally covered an area of roughly 45 ha and once extended as far as 950 m from the mountain front. The fan constructed at the mouth of the much smaller PML-containing watershed appears to have covered an area of about 9 ha, extended up to 550 to 600 m from the mountain front, and impinged upon the ML's southerly lateral levee over a distance of about 250 m (Figure 1).

Based on the geomorphology of the PML, we estimate that erosion has removed approximately 6×10^5 m³ of debris from its host canyon since emplacement. If this erosion occurred within a short time and transferred the entire volume to the proximal fan, it would have produced a postevent alluvial deposit with an average thickness of about 6 to 7 m. More likely, the rate of debris production started off high but tapered off over time. Based on the geomorphology of the fan and comparing with the thickness of the deposits at the mouth of the MSC, we consider it more likely that the PML's proximal fan never exceeded a thickness of about 5 to 6 m at the mouth of the canyon, tapering to smaller values towards the edges.

Following deposition of the proximal fans, the MSC and PML fan heads experienced approximately 25 m and 2 to 5 m of incision, respectively. We ascribe this incision to recovery from the short-term effects of the landslide, coupled with adjustment to unrelated climatic and/or tectonic factors that have affected all the canyons and alluvial fans along this portion of the mountain front. During this period of incision, erosion almost completely removed the ML's northern lateral levee along with portions of the DH. Similarly, stream flows from the PML canyon eroded much of its proximal fan, breached the southern lateral levee at the mountain front, incised the southerly margin of the MSC's abandoned proximal fan, and scoured alluvial material from the northerly side of the levee (Figure 1).

As discussed previously, the interior base of the levee currently lies about 10 m below its south-facing exterior at most locations (Figure 1). Potential explanations for this elevation difference include (1) scour of the alluvial surface by the ML during emplacement, (2) preferential postemplacement ero-

sion of alluvium from the inner margin of the levee, and/or (3) preferential deposition of alluvium along the outside of the levee.

A scour origin for the elevation differential is conceptually straightforward and requires no substantial postemplacement elevation changes to the adjacent alluvial landforms. It also explains the 100 m widening and apparent volume increase of the DH upon exiting the MSC. Hence, the geomorphology of the ML and DH are consistent and compatible with a scour origin for the present configuration of the lateral levee and is our preferred interpretation.

The presence of alluvium of unknown depth bracketing the intact lateral levee complicates this simple geomorphic interpretation. Regarding the possibility that the lower interior level of the levee results from postemplacement fluvial scour, we note that landslide breccia is exposed to within 1 to 2 m of the base of the interior slope of the levee, thus indicating that the inner side of the levee extends to a depth of at least 8 to 9 m below the exterior alluvial surface. Hence, the elevation differential between the opposing sides of the levee is not attributable to preferential erosion of alluvium on its inner side.

Regarding the alternative possibility, i.e., that the elevation differential between the opposite sides of the levee reflects aggradation along the southerly side of the embankment, we cite the following observations:

(1) Proximal levee Profiles E and F (Figure 1) abut bedrock outcrops and are definitively unaffected by external aggradation, yet they exhibit geometries quite like Profiles A-C lower on the fan (Figure S25)

(2) The alluvial fan associated with the PML watershed abuts the levee section that exhibits the greatest inside-to-outside elevation differential, yet this watershed is much smaller and lower in elevation than the MSC. This indicates, *a priori*, that sediment production from the PML watershed must be significantly less than from the MSC, a fact inconsistent with much greater depths of alluviation on the PML-fed side of the levee

(3) Just below the mountain front, the PML watershed constructed a proximal fan that appears to have banked up against a 250 m long section of the levee following emplacement of the landslide (Figure 1). Flows from the PML watershed subsequently reworked much of this fan and, along with activity along the range-front fault, opened a 50 m wide gap in the levee and triggered ~1 to 2 m of incision on both sides of the levee. Based on the sum of our observations, we conclude that as much as 5 m of aggradation occurred outside the levee in the vicinity of Profile D (Figure 1) following emplacement of the slide and as much as to 4 m of this material remains in place today (Figure 1, Profile D). This aggregation is localized to the area near the mountain front and fails to explain the 10 m inner/outer elevation contrast observed along most parts of the levee
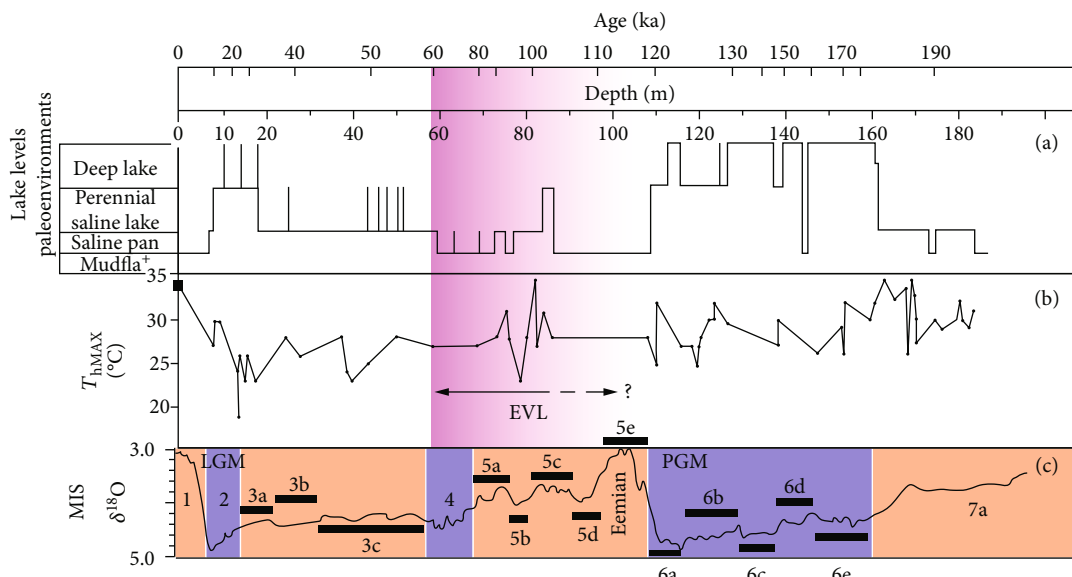
FIGURE 3: Estimated date range for the EVL (pink shading) projected on Death Valley pluvial reconstructions (a) and estimated maximum water temperatures (b) derived from sediment cores [38]. Also shown are marine oxygen isotope (MIS) stages and substages and $\delta^{18}O$ values for the past 200 ka [39]. Relatively warmer intervals are highlighted in orange, cooler periods in blue. Also indicated are the time of the last glacial maximum (LGM), the penultimate glacial maximum (PGM), and the Eemian interglacial period.

(4) At the distal end of the levee, the preserved headscarp stratigraphy exposed at Location X (Figure 1) implies that the base of the landslide currently lies around a meter below the base of the field exposure (Table 6), a finding inconsistent with significant postemplacement aggradation or erosion of the fan surface in this area. These relations imply that the Dedeckera Canyon alluvial fan, which abuts this part of the ML (Figure 1), lies at approximately the same grade today as it did at the time of emplacement of the EVL

Based on these observations and the appearance of the levees in the field, we are of the opinion that a 10 m aggradation event affecting the entire southern side of the ML is highly unlikely, that the exposed exterior base of the levee more likely lies within 0 to 4 m of its original deposited position, and that the lower relative elevation of its north side principally reflects the effects of scour by the ML during emplacement of the landslide.

5.5. Age. Well-developed desert pavements, pitted carbonate clasts, and dark brown varnish on noncarbonate clasts characterize the alluvial surfaces overlying the EVL, providing a minimum age estimate of ~60-80 ka for the deposit [25]. Rough constraints on its maximum age are provided by the character of lacustrine deposits formed near the head of the PML (Figure 1, Feature 3), which formed in response to temporary blockage of local drainage courses by landslide debris. The absence of strong carbonate cementation in these deposits limits their age to roughly 100 ka [36].

Figure 3 compares the estimated age range of the EVL with local and global paleoclimatic records over the past 200 ka. Pluvial conditions prevailed in nearby Death Valley at various points during this period, particularly between 10 and 35 ka (marine oxygen isotope stage 2), circa 102 ka (MIS 5c), and between 120 and 186 ka (MIS 5e/6), when the valley supported perennial lakes (collectively "Lake Manly"). These pluvial periods likely correspond with the occurrence of other large-scale late Pleistocene lakes in the Great Basin, including Bonneville, Lahontan, Deep Springs, Fish Lake, Owens, and Searles [35]. In notable contrast, no geologic evidence exists to suggest that the Eureka Valley supported perennial lakes at any point during the Quaternary period [37]. Somewhat dryer but still wetter-than-present conditions prevailed from 35 to 60 ka (MIS 3-4) and between 85 and 102 ka (MIS 5b/c) when Death Valley supported one or more ephemeral saline lakes [38, 39].

Based on a minimum age of ~60-80 ka, the presence of the playa deposits impounded by the EVL with a maximum age of ~100 ka and the pluvial history of Death Valley, we tentatively assign the lacustrine deposits at the head of the PML to MIS 5b/c at 85-102 ka and the slide itself to an earlier date, perhaps extending as far back as the Eemian interglacial (MIS5e). It appears doubtful that the EVL could predate the Eemian, as sedimentary deposits formed during the penultimate pluvial period (MIS 6) should exhibit notable carbonate sedimentation not observed in sediments associated with the EVL.

5.6. Runout of Debris. For the purposes of the following discussion, we initially address the kinematics of landslide runout, followed by an evaluation of its detailed dynamics. Kinematics describes motion "from the standpoint of measurement and precise description," whereas dynamics is concerned with "the causes or laws of motion" [40]. In other words, kinematics describes what happened, and dynamics describes why it happened. Too frequently, these issues have been comingled in the technical literature of long-runout

landslides since Heim [16]. As such, we make every effort to segregate these issues here.

5.6.1. Kinematics

(1) Effective Coefficient of Sliding Friction. Heim [16] introduced the concept of the fahrböschung as a semiquantitative measure of the relative efficiency of long-runout landslide transport and emplacement. He defined this measure as the angle of a line connecting the crown of the headscarp with the toe of a long-runout landslide and promoted its use as a surrogate for the angle of the line connecting the initial and final positions of the landslide center of mass, in practice a difficult value to determine. As described previously, Hsü [2] in turn promoted the use of the tangent of the fahrböschung, the ratio of the fall height (H) to runout length (L) as a method to compare the relative mobility of long-runout deposits.

Among the more enigmatic characteristics of long-runout landslides as a group is their trend towards decreasing H/L ratios with increasing volume following a log-normal relationship, first noted by Scheller [41]. Shaller [9] extended this analysis by breaking out various groupings of long-runout landslides by their degree of confinement, lithology, and other factors. In general, the ML and PML fall within the trend of the larger population of long-runout landslides in H/L vs. Log(Volume) space and close to the regression line for unconfined landslides, indicating that they exhibit similar mobility to these landslides despite being channeled for the majority of their runout. They also exhibit modestly greater mobility than the family of carbonate landslides and somewhat lesser mobility than the terrestrial population of terrestrial Blackhawk-like landslides (not applicable to the PML, which does not share this morphology; Figure S26).

(2) Velocity. Based on a review of aerial images projected onto Google Earth topography, it is possible to estimate the velocity of the EVL at three locations where debris overtopped watershed boundaries (assuming the current topography approximates that present at the time of landslide emplacement), as shown in Figure 1. We developed velocity estimates at these three points by assuming conversion of kinetic energy into gravitational potential energy using the following formula [42]:

$$\frac{1}{2}mv^2 = mgh, \tag{1}$$

$$v = \sqrt{2gh}, \tag{2}$$

where m is the mass (kg), v is the velocity (m/s), g is the gravitational acceleration (m/s^2), and h is the height of an overtopped obstacle (m).

Equation (2) represents a "best guess" velocity estimate because it (1) assumes perfect conversion of kinetic energy to gravitational potential energy (thus underestimating true velocity), while (2) failing to account for potential momentum transfer between leading and trailing portions of a moving landslide (thus possibly exaggerating the velocity estimate).

The first overtopping point is located where the PML entered its side canyon, accompanied by an elevation rise of approximately 35 m. The second point is where PML debris overtopped a second, 20 m high watershed boundary. The third overtopping point is located along the northern edge of the ML runout track where landslide debris spilled over the divide with the neighboring watershed to the north. This divide stands approximately 90 m above the floor of the MSC.

Applying Equation (2), the calculated velocity of the debris at the first, second, and third overtopping points is ≥26 m/s, 20 m/s, and 42 m/s, respectively (Figure 1). These velocity estimates lie towards the lower end of the 20 to 100 m/s range reported for 57 terrestrial subaerial long-runout landslides by Shaller [9].

(3) Spreading of Landslide Mass. We estimate that the slide block that contributed mass to the final EVL deposit originally measured approximately 300 m wide by 386 m long by 35 m thick (applying the conclusion that the ML scoured its base during emplacement). Once displaced from the mountainside, the fragmented slidemass encountered a bedrock ridge that split the debris into two principal components. Material that passed to the north of the ridge and ultimately exited the canyon comprised about 60% of the original mass; the remainder moved south to form the PML. Accordingly, approximately the northerly 180 m of the detached slide block contributed to the ML and the southerly 120 m to the PML. By the time the ML debris reached the mouth of the MSC, it measured about 300 m wide and 15 m thick. Relative to the dimensions of the initial source block, this represents a widening of about 175% and a thinning of about 60%. If we assume that the detached slide block experienced 25% bulking during its transit of the MSC, the slidemass would have extended to a length of 675 m by the time it exited the canyon. Notably, this value is approximately equivalent to the final length of the DH.

(4) Preservation of Attenuated Headscarp Stratigraphy. The preservation of headscarp stratigraphy in attenuated form is obvious along the southern margin of the ML. It also occurs in one of the northerly side lobes (Figure 1, Location 8) and may exist in the PML. Despite fragmentation of the originally intact limestone block during its descent from the mountainside, these preserved stratigraphic relations indicate that the landslide experienced remarkably little vertical mixing and therefore a very low vertical velocity gradient during runout. We therefore infer that most of the relative movement between the landslide debris and the substrate occurred at or near the base of the landslide (i.e., the landslide slid and did not flow into place).

The ~40 : 1 attenuation of source area stratigraphy preserved in exposures along the southerly margin of the ML (Table 6) places additional constraints on the kinematics of emplacement. The teardrop-shaped DH experienced about 1.5x longitudinal and 2.2x lateral extension by the end of movement, implying that the bulk of the deposit should
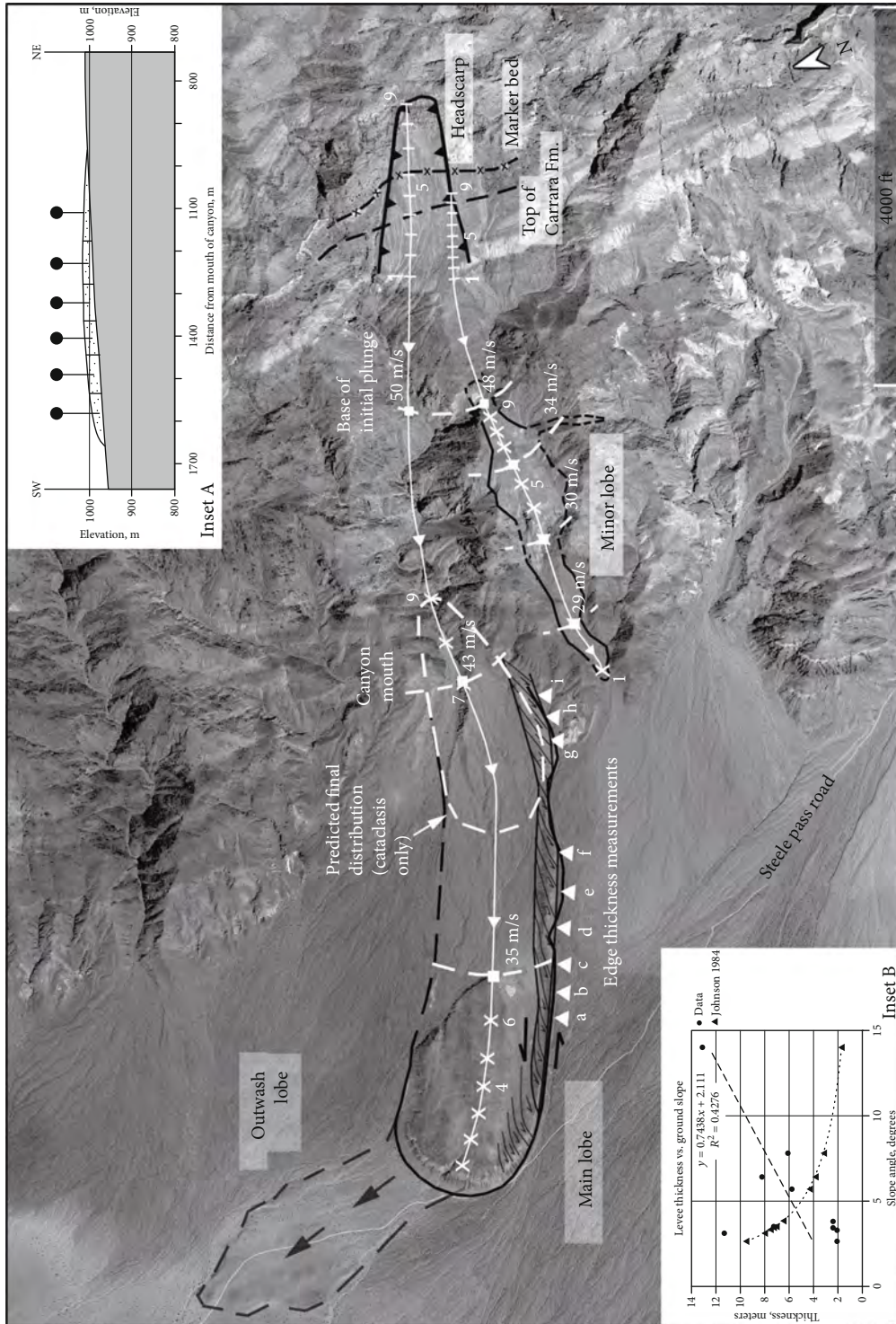
FIGURE 4: Schematic depiction of proposed structural mechanism responsible for extreme attenuation of stratigraphy along the southerly lateral levee during runout (black lines and arrows). Also shown are the results of application of the cataclasis and hybrid models of landslide runout discussed in text. Numbered dashes in the headscarp area show the starting locations of individual slide blocks, X's mark calculated final locations. Velocity estimates shown for the leading edge of main and minor lobes at various points along their respective runout paths. Locations of possible outwash lobe and key stratigraphic horizons shown by dashed lines. Inset A shows a cross section through the distal heap, subdivided into equal areas for estimation of final block locations as applied to hybrid model calculations. Inset B shows plot of anticipated deposit thickness vs. slope angle for a material exhibiting a plastic rheology (dotted line) vs. actual conditions (dashed) measured along southerly lateral levee. Locations a–i indicate locations of levee thickness and alluvial slope measurements.

exhibit an approximate attenuation factor of $1.5 \times 2.2 \approx 3 : 1$, less than one-tenth the amount exposed along its southern margin.

We propose that the extreme attenuation observed along the eroded southerly edge of the deposit is a boundary effect resulting from shear between the rapidly moving interior and the outer edge of the ML, manifested in the manner of an imbricate thrust sheet laid on edge (Figure 4). Shaller [20] described an analogous texture from the Carlson landslide, Idaho, where large, distinctive, isolated blocks of volcanic agglomerate derived from a unique source area in the headscarp exhibit a "string of pearls" arrangement along one lateral levee due to focused longitudinal extension along the margin of the deposit. Lava flows are known to develop similar marginal shear zones and lateral levees [43]. These observations support the hypothesis that longitudinally attenuated marginal shear zones such as that documented along the margin of the ML may be a common characteristic of moving bodies of soil and rock.

(5) Incorporation of Alluvial Substrate. As described above, our preferred geomorphic interpretation is that the ML scoured and incorporated up to 1.6 million m^3 of alluvium during its descent of the alluvial fan below the mouth of the MSC, a volume that corresponds to approximately 34% of the total volume of the ML and 37% of the volume of the DH. Entrainment of alluvial substrate material is known or suspected to have accompanied the emplacement of long-runout landslides elsewhere, with the scoured material representing from ~15% [44] to ~820% [27] of the original bulked volume of landslide debris. Based on field observations and experimental debris flow bed scour analyses by de Haas and van Woerkom [45], potential reservoirs of displaced alluvium in the main lobe include (1) accumulation in a bulldozed distal wedge; (2) bulk interleaving of alluvium with carbonate landslide debris; (3) underplating; and (4) fine intermixing with the carbonate breccia. We estimate the maximum volume of a potential bulldozed wedge to be about 10^5 m^3, suggesting that the other listed reservoirs represent more likely repositories of the scoured material, consistent with the comingled appearance of landslide debris and alluvium along the eroded northern edge of the ML.

(6) Kinematic Wave Behavior. The longitudinal profile of the DH resembles a breaking wave, with a steep leading edge that tapers in the upslope direction. This profile resembles wave-like impulses elsewhere, including natural phenomena such as debris flows [46]. In general, this geometry arises when more rapidly moving trailing material overtakes the leading edge of a sliding or flowing material. The presence of at least one steeply dipping reverse fault in the DH supports the premise that the leading edge slowed relative to trailing material near the conclusion of runout, resulting in compression between these portions of the slide mass. Possible explanations for the appearance of this feature in the DH include (1) resistance to advancement as a result of bulldozing of a passive wedge of alluvium before the DH (Figure 1, Transect G) and/or (2) progressive downslope reduction in the slope of the alluvial surface, which would affect a slowdown in

the leading edge of the slide before the trailing material encountered the same lower slopes.

5.6.2. Dynamics. Based on the preceding observations and analysis, we hypothesize three fundamental processes to explain the key characteristics of the EVL. The first and principal of these processes is particle fracture (cataclasis) with energy recycling, which we envision controlling the dynamics of the landslide during its transit of the bedrock canyon areas. The other processes, applicable to the ML as it transited the alluvial fan at the mouth of the MSC, include incorporation of substrate material and localized liquefaction of the alluvial substrate.

(1) Proposed Particle Fracture (Cataclasis) with Energy Recycling Mechanism. Rather than representing a mere by-product of emplacement, we interpret slidemass brecciation to be a key process underlying the long-runout phenomenon in the EVL, particularly during its transit of the bedrock canyon areas. We view clast breakage as partially interrupting the process of frictional energy dissipation within and along the base of the moving landslide during runout. In this regard, the proposed mechanism is broadly analogous to previously hypothesized mechanisms that invoke acoustic or mechanical grain flow mechanisms to limit frictional energy losses and extend the reach of large-scale landslides via high frequency intergrain and grain-to-substrate impacts [2, 47–49]. From a geological standpoint, the principal drawback to these grain flow mechanisms is their failure to explain the textures of these deposits [17], specifically (1) grain flow models require that clasts remain intact through the collisional process, whereas field evidence suggests that clast fragmentation is pervasive inside rapidly moving landslides, even to the finest scales (Figure S27 and Figure S28) [9, 50]; and (2) these mechanisms should produce deposits rich in rounded particle shapes, normal grading, and other textural features common to known geo-logic grain flow processes such as turbidity currents [51] and pyroclastic sediment gravity flows [52] but largely absent in the EVL and other long-runout landslides.

The cataclasis model proposed herein is, in contrast to these other models, consistent with and indeed motivated by the observed texture of the EVL and other long-runout landslides. In this model, the kinetic energy applied to the basal clasts in contact with each other and with the substrate commonly results in their rupture (rather than rebound), thus recycling the elastic strain energy momentarily stored in these clasts back to the landslide in the form of spherical shock waves. Such shock waves would rapidly propagate through the slide mass at a velocity of ~100-1200 m/s [53, 54], substantially faster than its maximum runout speed, thus communicating the effects of clast breakage quickly throughout the body of a rapidly moving landslide.

For this proposed mechanism to function, impact rupture must occur throughout the course of runout (or major portions thereof), not just during rare or singular occurrences such as the impact of the slidemass at the base of its initial plunge, as proposed by Shreve [10] for the Blackhawk landslide. While some slidemass brecciation (or
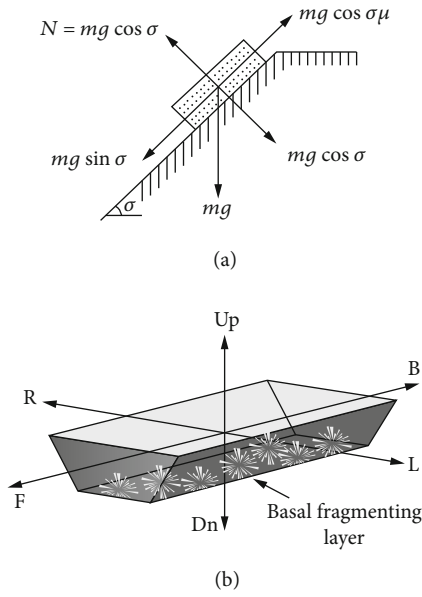
FIGURE 5: (a) Depiction of forces associated with kinematics of block-on-inclined-plane model, where m is the mass (kg), g is the gravitational acceleration (m/s²), σ is the slope angle (deg.), μ is the frictional coefficient (dimensionless), and N is the normal force (N). (b) Conceptual model of clast fragmentation near the base of a rapidly moving landslide. Landslide movement is from right to left. Directional arrows defined as follows: F: forward; B: back; L: left; R: right; Up: up; Dn: down.

disarticulation along existing discontinuities) likely accompanied the EVL's initial plunge from the headscarp, the character of small-scale landslides and rockfalls tells us that in the absence of some other process, this initial phase of movement would result in a mixed and ungraded mass of rubble at the foot of the source slope. The preservation of headscarp stratigraphy and reverse grading in the EVL instead implies the action of another, far less chaotic, process that operated along the base of the landslide from the outset of the event. We envision focused basal fragmentation of the moving slide-mass to be this mechanism.

(2) Block-on-Inclined-Plane Analysis. The block-on-inclined-plane model is a simple but powerful representation of landslide runout (Figure 5(a)). In the basic model, the acceleration, a (m/s²), of a block of mass m (kg), is dependent on the difference between the driving forces ("mg sin σ" term) and the resisting forces ("mg cos σ μ" term):

$$ma = mg \sin \sigma - mg \cos \sigma \mu, \qquad (3)$$

which simplifies to:

$$a = g (\sin \sigma - \cos \sigma \mu), \qquad (4)$$

where σ is the slope angle (degrees) and μ is the coefficient of sliding friction.

In this treatment, we view the proposed cataclasis mechanism as acting through a modification of the resisting term

in Equation (3), which represents the energy dissipation of a landslide block sliding on its bed if taken on a per meter basis (i.e., as work). For purposes of quantification, we approach this problem by resolving the impulse energy from hypothesized breakage-induced shocks into three perpendicular axes relative to the travel direction: vertical, lateral, and longitudinal (Figure 5(b)). Similar to the effects that result from grain collisions in mechanical grain flow simulations [2, 47–49], we envision that the vertical component of the impulses acts to reduce the effective normal force of the landslide on its bed, thereby reducing the effective frictional coefficient of the landslide. The lateral component, in turn, acts to potentially spread the debris normal to the movement direction. The longitudinal component acts to both accelerate the leading edge and slow the trailing edge of the landslide relative to the center of mass, resulting in an increase in the runout length of the leading edge and extending the debris sheet in the longitudinal direction.

Assuming conversion of the frictional work into rock breakage instead of heat permits calculation of the magnitude of the six force vectors depicted on Figure 5(b) by partition of the "mg cos σ μ" term into six orthogonal vectors of equal magnitude:

$$\text{Up} = \text{Dn} = \text{R} = \text{L} = \text{F} = \text{B} = \left(\frac{1}{6}\right) mg \cos \sigma \mu. \qquad (5)$$

Recognizing that perfect conversion of the resisting force to rock breakage is unlikely, an efficiency term, ε, with a value between 0 and 1, is added to Equation (5) for completeness:

$$\text{Up} = \text{Dn} = \text{R} = \text{L} = \text{F} = \text{B} = \left(\frac{1}{6}\right) \varepsilon mg \cos \sigma \mu. \qquad (6)$$

In addition to frictional losses, ε is expected to depend on factors such as the thickness, velocity, rock strength, and dilation of the rock mass due to fragmentation. While not treated here, we expect the efficiency of clast breakage to increase with velocity and basal loading and decrease with increasing rock strength. Landslides on bodies with lower gravitation should therefore be less efficient than those on Earth because of reduced velocity and basal loading, consistent with the observed behavior of Martian landslides [55].

Applying Equation (6) to the standard block-on-inclined-plane model, we obtain the following modified relationship for the acceleration of the center of mass (a_{CM}) assuming the effect of cataclasis and instantaneous rebound of the downward-directed vector from the bedrock surface upwards into the moving mass:

$$ma_{CM} = mg \sin \sigma - [mg \cos \sigma \mu - \text{Up} - \text{Dn}],$$

$$ma_{CM} = mg \sin \sigma - \Big[mg \cos \sigma \mu$$
$$- \left(\frac{1}{6}\right) \varepsilon mg \cos \sigma \mu - \left(\frac{1}{6}\right) \varepsilon mg \cos \sigma \mu\Big], \qquad (7)$$

which simplifies to:

$$a_{CM} = g \left[\sin \sigma - \cos \sigma \mu \left(1 - \left(\frac{1}{3} \right) \varepsilon \right) \right]. \qquad (8)$$

Applying the same methodology to the leading edge of the landslide (a_{LE}), we have:

$$ma_{LE} = mg \sin \sigma - [mg \cos \sigma \mu - Up - Dn - F],$$

$$ma_{LE} = mg \sin \sigma - \left[mg \cos \sigma \mu - 3 * \left(\frac{1}{6} \right) \varepsilon mg \cos \sigma \right], \qquad (9)$$

which simplifies to:

$$a_{LE} = g \left[\sin \sigma - \cos \sigma \mu \left(1 - \left(\frac{1}{2} \right) \varepsilon \right) \right]. \qquad (10)$$

Similarly, the acceleration of the trailing edge of the landslide (a_{TE}) is:

$$ma_{TE} = mg \sin \sigma - [mg \cos \sigma \mu - Up - Dn + B], \qquad (11)$$

$$ma_{TE} = mg \sin \sigma - \left[mg \cos \sigma \mu - 2 * \left(\frac{1}{6} \right) \varepsilon mg \cos \sigma \mu \right.$$
$$\left. + \left(\frac{1}{6} \right) \varepsilon mg \cos \sigma \mu \right], \qquad (12)$$

$$a_{TE} = g \left[\sin \sigma - \cos \sigma \mu \left(1 - \left(\frac{1}{6} \right) \varepsilon \right) \right]. \qquad (13)$$

Following similar reasoning, Equations (14) and (15) provide accelerations to the right (R) and left (L) of the main travel path in the transverse direction (TR):

$$a_{TR,R} = g \left[\sin \delta_R + \mu \left(\frac{1}{6} \varepsilon \cos \sigma - \cos \delta_R \right) \right], \qquad (14)$$

$$a_{TR,L} = g \left[\sin \delta_L + \mu \left(\frac{1}{6} \varepsilon \cos \sigma - \cos \delta_L \right) \right], \qquad (15)$$

where δ_R and δ_L are the slopes to the right and left perpendicular to the main direction of travel. By inspection, lateral spreading is generally not anticipated to occur by way of the cataclasis mechanism except in unusual cases in which the transverse slope angle approximates the slope angle in the main travel direction.

In summary, the kinematic equations applicable to the leading edge (LE), center of mass (CM), trailing edge (TE),

and transverse (TR) spreading of a moving landslide experiencing basal rock fragmentation are as follows:

$$a_{LE} = g \left[\sin \sigma - \cos \sigma \mu \left(1 - \left(\frac{1}{2} \right) \varepsilon \right) \right],$$

$$a_{CM} = g \left[\sin \sigma - \cos \sigma \mu \left(1 - \left(\frac{1}{3} \right) \varepsilon \right) \right],$$

$$a_{TE} = g \left[\sin \sigma - \cos \sigma \mu \left(1 - \left(\frac{1}{6} \right) \varepsilon \right) \right], \qquad (16)$$

$$a_{TR,R} = g \left[\sin \delta_R + \mu \left(\frac{1}{6} \varepsilon \cos \sigma - \cos \delta_R \right) \right],$$

$$a_{TR,L} = g \left[\sin \delta_L + \mu \left(\frac{1}{6} \varepsilon \cos \sigma - \cos \delta_L \right) \right].$$

For the end-member case of $\varepsilon = 0$, the equations simplify to a basic block-on-inclined-plane analysis. For any value of $\varepsilon > 0$, an additional factor is necessary to account for the volume change associated with brecciation of the slide mass (25% volume increase divided by the six cardinal directions). The theoretical maximum value of ε is therefore slightly greater than 1.

Following the reasoning in Figure 5(b), we expect the pressure waves produced by the rupturing rock debris to dilate the basal portion of the moving debris, much as acoustic and collisional processes induce dilation near the base of nonfragmenting grain flows [2, 47–49]. Indeed, given the multiplicity of grain interactions occurring near the base of a rapidly moving landslide, nonfragmental grain collisions and their associated phenomena likely contribute in some subsidiary way to the mechanics of these mass movements, a conclusion perhaps supported by the presence of sub-rounded clasts in the EVL.

In addition to explaining the texture and the detailed kinematics of the EVL, the basal fragmentation mechanism also helps explain the observed lack of spattering of rock beyond the limits of the landslide. This is because the cataclasis mechanism and its associated rapid grain motions are expected to primarily occur along the base of the thick, central portion of the moving landslide and not beneath its thinner and slower moving margins.

(3) Supporting Observations. For the cataclasis model to function, impact rupture must occur for the duration of runout (or major portions thereof), not just during rare or singular occurrences such as the impact of the slidemass at the base of its initial plunge. Beyond the EVL's textural characteristics, support for the cataclasis model is available from the mineral processing and aggregate testing fields as well as from the deposits of other long-runout landslides. Specifically:

(1) The potential energy released by the falling slidemass was more than sufficient to pervasively fragment the source block during runout

(2) Slidemass fragmentation along preexisting disconti-nuities and via impact-induced tensile and shear

failures is reasonable under the conditions prevailing at the base of the rapidly moving landslide

(3) Limestone toughness estimates (the energy absorbed by a rock during fracture propagation) are consistent with impact fragmentation during runout

(4) Hysteresis effects lower the resistance of limestone clasts to impact fragmentation, thus extending the reach of the mechanism to flatter slopes and lower speeds

(5) Microtextural observations from other long-runout landslide provide additional support for the cataclasis mechanism

(4) Energy Considerations. The energy requirements for clast breakage derived from the mineral processing literature provide independent (i.e., nontextural) support for the envisioned cataclasis mechanism. In mineral processing, the prediction of energy consumption in a jaw crusher during the size reduction process is commonly estimated using the Bond relationship [56]:

$$W = 10B\left(\frac{1}{\sqrt{P_{80}}} - \frac{1}{\sqrt{F_{80}}}\right), \qquad (17)$$

where B is the Bond index (kWh/1000 kg), P_{80} is the size (in microns) at which 80% of the product passes, F_{80} is the size (in microns) at which 80% of the feed passes, and W is the energy consumption (kWh/1000 kg). For limestone, $B = 12.8$ kWh/1000 kg [56]. Per Equation (17), the crushing of 6 cm ($F_{80} = 60,000$ microns) limestone feed stock to 2.5 cm ($P_{80} = 25,000$ microns) product would require an energy input of 0.287 kWh/1000 kg ≈ 1 kJ/kg. Similarly, the crushing of 20 cm feed stock to 6 cm rock would require an energy input of ~0.8 kJ/kg. Because the efficiency of comminution equipment is typically less than 10% [57], the actual energy input to the feed stock needed to produce the example particle size reductions is probably about 0.1 kJ/kg, approximately equal to the gravitational potential energy released by a fall of 10 m per kilogram. By comparison, the center of mass of the main lobe experienced an elevation drop of over 500 m between the source area and the mouth of the MSC. Hence, even if the comminution process in the EVL was only as efficient as a jaw crusher, the gravitational potential energy released by the slidemass during emplacement would have been capable of carrying out the example size reduction five times over per kilogram of landslide debris. These observations are consistent with substantial rock breakage during runout from an energy perspective.

(5) Strength Considerations. In addition to energy considerations, it is also necessary to demonstrate that the EVL's constituent rock fragments could reasonably experience impact fragmentation in the environment of a moving landslide. Clast strength is controlled by the strength of bedrock discontinuities, intact rock strength, and mineral hardness.

Because impact fragmentation is a dynamic process, dynamic rock strength represents the most important parameter for determining whether this process may reasonably occur in a moving landslide.

Published strength data for limestone, summarized in Table 9 [58–65], indicates that:

(1) Limestone is strongest in compression, with strength values one to two orders of magnitude higher than in shear or tension. The dynamic compressive strength is even greater, increasing linearly with impact load [60, 65]

(2) The static and dynamic shear strength of limestone are of similar magnitude, with the dynamic strength exceeding static values by no more than 25% [61]

(3) The dynamic and static tensile strength of limestone are roughly equivalent [62]

(4) As expected, the shear strength of limestone discontinuities is very low, roughly one to two orders of magnitude below that of intact rock [58]

In summary, the relative dynamic strength measures for limestone rank as follows:

$$\text{Discontinuities} << \text{Tensile strength} \approx \text{Shear strength} \\ << \text{Compressive strength} \qquad (18)$$

Clast fragmentation requires the imposition of impact forces that exceed the minimum strength of the constituent clasts. Hence, based on the preceding strength ranking, we surmise that fragmentation would initially involve disarticulation of the rock mass along preexisting discontinuities, followed by breakage of intact clasts via shear or tensile failure. In the context of a rapidly moving landslide, failure in shear is expected to result from tangential/glancing blows, whereas tensile failure is hypothesized to occur by means of clast impacts sufficiently energetic to "split" the rock normal to the impact load (Figure S29). The latter failure mode is analogous to that in the standard Brazilian tensile strength test [66].

Dynamic failure of limestone by shear or tensile fracture would entail the application of an impact pressure of at least 4 MPa to a target clast, which is readily achievable inside a rapidly moving landslide. To illustrate, we consider the following hypothetical: a 1 kg clast impacts another rock fragment at a relative velocity of 40 m/s with a contact time of 0.1 s, yielding an impact force of 400 N. Application of this force to an area of 1 cm^2 results in a force per unit area of 400 N/0.0001 m^2 or 4 MPa. If the clasts rebound from one another or from the substrate after impact, the applied force/area would be double this value. More than likely, clast fragmentation is driven by localized concentrations of pressure on individual clasts caught at the basal contact between a large mass of moving debris and the stationary substrate (especially bedrock).

(6) Toughness Considerations. Rock strengths, such as the tensile and shear strength, are one measure of its resistance

TABLE 9: Static and dynamic strength values for limestone.

Strength measure	Strength (MPa)			
	Static	Dynamic (initial)	Dynamic (10^3 cycles)	Dynamic (10^5 cycles)
Compressive strength	50–200 [61]	~75–300 [63]	~56–225 [66]	~53–210 [66]
Shear strength				
Intact	3-7 [61]	~4–9 [64]	~3–8 [67],1	—
Discontinuities	0.05-0.2 [62]			
Tensile strength	4–20 [61]	4–20 [65]	~2–10 [66]	~1–5 [66]

[1]Estimated from tuff and artificial sandstone materials.

to brittle failure. Another measure of rock resistance to brittle failure is the energy absorbed by the rock during fracture propagation, referred to as material toughness. The Los Angeles Abrasion (LAA) test is the standard test method for evaluating rock toughness. For coarse aggregate (>19 mm), the test involves revolving 10 kg of dry material together with twelve steel balls collectively weighing 5 kg in a 70 cm diameter drum for 1000 revolutions at 30 to 33 rpm [67]. A fin in the drum lifts the rock and steel balls, allowing them to tumble down onto the material below, creating an impact-crushing effect. After the prescribed number of revolutions, the contents are removed, the aggregate portion is sieved to remove all material finer than 1.7 mm, and the remainder weighed. The final weight divided by 10 kg gives the sample attrition.

The peak velocity achieved by the 0.42 kg steel balls typically used in the LAA apparatus is approximately 3.3 m/s or less, associated with a freefall distance of about 55 cm and an impact energy of about 20 J. The published LAA test results for limestone and dolomite indicate that after 1000 cycles, these materials experience significant impact attrition, with attrition rates that range from 24 to 36% [67, 68]. Given the much higher velocity of the EVL (often over 40 m/s) and the long distance of travel (over a kilometer across rugged, exposed bedrock), the accumulation of thousands of impacts with energies in excess of 20 J appears likely in the constituent debris. Hence, the results of the LAA test imply a high likelihood of impact fragmentation of limestone and dolomite rock types in the moving landslide during runout from a toughness perspective.

(7) Hysteresis Effects. Prolonged cyclic loads reduce rock strength due to the accumulation of microfractures in the affected material. For all rock types, test methods, and failure types, Cerfontaine and Collin [69] report a steady reduction in rock strength with the number of accumulated load cycles, with strengths diminishing by about 15% after 10^3 load cycles and 22% after 10^6 cycles. For the special case of limestone, Haimson [63] reported 50 to 75% reductions in tensile strength and 25 to 30% reductions in compressive strength following application of 10^3 to 10^5 load cycles. Kamonphet et al. [70] report no notable reductions in limestone shear strength over a course of 10 shear cycles, while Okada and Naya [64] report a 15 to 20% reduction in the shear strength of tuff and artificial sandstone following application of 10^3 load cycles (Table 9).

Although the number of load cycles experienced by the clasts in a rapidly moving landslide is difficult to judge, movement over a rugged landscape should induce many load cycles in the affected clasts, perhaps as many as one per meter of travel or more. At a speed of 40-50 m/s, this would imply 40 to 50 cycles per second and the accumulation of between 10^4 and 10^5 load cycles per kilometer of travel. Seismic recordings of rapidly moving landslides have documented frequencies in the 40-50 Hz range [71], supporting the hypothesis that load cycles accumulate rapidly in such events.

(8) Microtextural Considerations. In extremely energetic landslide environments, clast breakage is followed by the breakdown of the individual mineral grains [9, 50]. In common rock durability tests such as the Los Angeles (ASTM C 535, LAA) and mill abrasion tests, this process is controlled by mineral hardness [67]. It is unknown whether this process took place in the EVL. The process is, however, known from other examples, including the Martinez Mountain [9] and Travertine [50] landslides of southern California. In both examples, petrographic analysis of fine, coherent samples of rock breccia from the base of these landslides captured "freeze frame" images of individual mineral grains in the act of fragmenting and dispersing in a fine-grained matrix. The imagery from these petrographic analyses provides a visual guide to the functioning of the comminution process at work in these landslides and helped inform the comminution mechanism envisioned herein.

(9) Application of the Cataclasis Model to the Eureka Valley Landslide. To test the proposed cataclasis model for the EVL, we applied Equations (8), (10), and (13) to simplified runout path geometries for the ML and PML derived from Google Earth topography (Table 10). As shown in Table 10, the modeled runout path geometry for the ML consists of seven segments of known length and slope angle, while eight segments were utilized to model the PML in recognition of its more sinuous travel path. Source blocks for the ML and PML were each subdivided into nine subblocks (numbered from lowest to highest on the source slope), whose center of gravity accelerations, velocities, and travel distances was followed in a spreadsheet calculation as they transited their runout paths. Initial block dimensions parallel to slope were taken as 31 m for the PML and 75 m for the ML calculations. Figure 4 shows the modeled travel path geometries, the locations of major break points, and the calculated starting and ending positions of the centroids of each of the subblocks.

TABLE 10: Modeled runout path geometries.

Segment	Starting elevation (m)	Final elevation (m)	Slope (degrees)	Ground length (m)	Notes
Main lobe					
High scarp	1844	1792	37	86	"Sacrificial" Bonanza King Formation
Upper upper headscarp	1792	1737	25	128	Scarp area upslope from white marker bed
Upper 1/2 headscarp	1737	1635	32	193	Top of interval corresponds with white marker bed
Lower 1/2 headscarp	1635	1545	28	193	
Initial plunge	1545	1310	29	490	
Main canyon	1310	1120	12	916	
Alluvial fan	1120	1006-965	5.5-7	930-1624	
Minor lobe					
Upper upper headscarp	1671	1660	27	24	"Sacrificial" material at base of Bonanza King Formation
Upper headscarp	1660	1610	24	124	Top of interval corresponds with top of Carrara Formation
Lower headscarp	1610	1565	21	124	
Initial plunge	1565	1334	30	462	
Antislope	1334	1369	-31	68.5	Top of antislope corresponds with wind gap at top of minor lobe
Upper canyon	1369	1278	13	413	
Lower canyon	1278	1154	15	473	
Canyon mouth	1154	1126	11	146	

Application of the cataclasis model entails calculation of variable accelerations for each of the in-tandem slide blocks, the magnitude of which depends on the gravitational acceleration, slope angle, and location relative to the other sliding blocks. Except in the immediate vicinity of slope transitions, Block 1 always experiences the greatest acceleration (Equation (10)) and the trailing block the lowest (Equation (13)), with intervening blocks experiencing intermediate values depending on the number of blocks in motion at any given time (Table 11). The start of a nine-block simulation utilizes the accelerations shown in the first row of Table 11. During a runout simulation, the trailing block, having the lowest acceleration, stops first. When the original trailing block (Block 9) comes to a halt, the accelerations of the remaining eight blocks shift to the second row in the table, and so on, until only Block 1 remains in motion. At this point in the simulation, the cataclasis mechanism is "shut off," and Block 1 is permitted to slide to a halt using an unmodified frictional coefficient, μ, equal to 0.5.

(10) Application to the Minor Lobe. Table 12 shows the results of application of the cataclasis model to the PML. The model results shown in the table apply for an efficiency factor, $\varepsilon = 0.88$, which provides a best match for the full suite of observed and inferred characteristics of the deposit. As noted in Table 10, the top of the minor lobe "Upper Scarp" corresponds to the upper contact of the Carrara Formation with the overlying Bonanza King Formation. This location was chosen because the Carrara Formation comprises nearly

TABLE 11: Acceleration factors for 9-block model.

No. blocks in motion	Block number								
	1	2	3	4	5	6	7	8	9
9	1/2	11/24	5/12	9/24	1/3	7/24	3/12	5/24	1/6
8	1/2	19/42	17/42	15/42	13/42	11/42	9/42	1/6	
7	1/2	8/18	7/18	1/3	5/18	4/18	1/6		
6	1/2	13/30	11/30	9/30	7/30	1/6			
5	1/2	5/12	1/3	3/12	1/6				
4	1/2	14/36	10/36	1/6					
3	1/2	1/3	1/6						
2	1/2	1/6							
1	0								

the entirety of the deposit. Though very little of the distinctively gray Bonanza King Formation limestone is present in the PML, a short additional "sacrificial" slope section is included in the calculations to account for the mass of slide material that must at one time have occupied the canyon area upslope from the minor lobe that has since been removed by erosion.

As shown in the second column of Table 12, the peak velocities of the nine PML starting blocks, calculated at the base of the "Initial Plunge" just below the headscarp, range

TABLE 12: Minor lobe runout calculations—cataclasis model.

Block no.	Starting elevation (m)	Peak velocity (m/s)	Runout distance from wind gap (m)	Est. final elevation top* (m)	Est. final elevation base† (m)	Est. thickness (m)
9	1671	26	1	1378	1368	10
8	1660	37	52	1387	1361	26
7	1646	39	111	1383	1348	35
6	1633	41	172	1367	1334	33
5	1615	43	236	1347	1315	32
4	1602	45	310	1330	1299	31
3	1590	46	426	1278	1267	11
2	1577	47	712	1190	1179	11
1	1565	48	900	1141	1141	0

*Elevation from Google Earth based on final computed location of each block. †Base elevation based on estimated preslide floor of the canyon from Google Earth and field observation.

TABLE 13: Main lobe runout calculations.

Block no.	Starting elev. (m)	Peak velocity (m/s)	Cataclasis model			Hybrid model		
			Est. final elev. (m)	Travel dist. (m)*	Canyon mouth velocity (m/s)	Obs. final elev. (m)	Travel dist. (m)ᵃ	μ_{AF}†
9	1844	49	1181	-297	NA	1181	-297	NA
8	1799	52	1151	-150	NA	1151	-150	NA
7	1764	55	1120	0	0	1120	0	NA
6	1731	55	1111	68	20	998	1109	0.13
5	1691	54	1103	134	27	990	1229	0.14
4	1652	53	1095	203	32	985	1322	0.14
3	1615	53	1084	285	36	979	1406	0.15
2	1580	52	1072	390	40	974	1492	0.16
1	1545	50	1059	493	43	969	1584	0.16

*Distance from the mouth of the canyon (at 1120 m elevation). †Calculated effective frictional coefficient for alluvial fan (AF) runout phase.

from 26 to 48 m/s. These velocity estimates meet or exceed the 26 m/s minimum velocity necessary for the landslide debris to climb the 35 m high opposing slope at the base of the initial plunge and enter the adjacent watershed. In the absence of the cataclasis mechanism or some other means of lowering the effective friction of the sliding rock, none of this slide material would have overtopped the wind gap and entered the adjacent watershed. For reference, Figure 4 shows the calculated velocity of the leading edge of the minor lobe at various points along its runout path.

In addition to the velocity estimates, both the overall length and the final mass distribution of the PML calculated using the cataclasis model are generally consistent with field evidence. Specifically, the cataclasis model predicts a distally tapered geometry, consistent with observations. The final profile geometry is obtained from the model by assuming that the initially 31 m long sliding blocks experience longitudinal spreading during runout to maintain contact with neighboring blocks; the farther the endpoints of neighboring blocks are to one another, the thinner the deposit.

(11) Application to the Main Lobe. The favorable results achieved by application of the cataclasis model to the PML suggest the model is reasonably applicable to the translation of a long-runout landslide through a bedrock canyon. Application of the cataclasis model to the runout of the ML resulted in the following findings:

(1) Conveyance of the white limestone marker bed from the mountainside to the mouth of the canyon and beyond by means of the cataclasis model requires a high efficiency factor—close to 1—as compared with the 0.88 value applied to the PML. Justification for the higher efficiency factor includes (a) the greater average thickness of the ML debris and (b) the lesser degree of bulk deformation accumulated by the ML during runout. The latter interpretation is based on the contrast between the well-preserved headscarp stratigraphy exposed in portions of the ML versus the major folding and deformation exposed in the interior of the minor lobe

(2) A trailing mass of material that did not itself exit the canyon is necessary to push material containing the white marker bed past the mouth of the canyon. The calculations suggest that the trailing edge of this missing slope section came to rest nearly 300 m upstream from the mouth of the canyon, as shown

in Table 13 and Figure 4. This trailing mass represents a volume sufficient to fill the lower end of the canyon to an average depth of about 15-20 m

(3) The velocity calculated for the leading edge of the ML at the mouth of the MSC (43 m/s) correlates well with the velocity calculated to have been necessary for the ML debris to overtop the watershed boundary to form the nearby northern minor lobe (42 m/s at Location 9 on Figure 1)

(4) The inferred kinematics of the transit of ML debris through the MSC are consistent with energy recycling via impact fragmentation and hysteresis of the constituent clasts

(5) The cataclasis model significantly underpredicts the final runout phase of the ML on the alluvial fan below the mouth of the canyon (Figure 4)

In view of these results, we consider the cataclasis mechanism capable of explaining the travel of the ML debris through the MSC. The exceptional mobility of the ML in traversing the alluvial fan, however, requires an alternative explanation based on the available field evidence, as outlined below.

(12) Hybrid Mechanism. When the ML exited the source canyon, it traveled approximately three times farther than predicted by the cataclasis model (and much farther still than a typical frictional coefficient would allow) while evidently bulldozing and incorporating 1.6 million m^3 of alluvium in its path. In the process, it developed a distally raised profile, distinguishing it from the tapered distal end of the PML. Based on these observations, we consider it unlikely that the cataclasis mechanism controlled the final runout phase of the ML. Instead, we hypothesize that the sudden imposition of load by the fast-moving landslide debris induced liquefaction of the alluvial substrate near the mouth of the MSC, triggering a process that controlled the subsequent movement of the landslide.

Several workers have posited substrate liquefaction during the emplacement of large, rapid landslides in more temperate environments, including Europe, Canada, Japan, and the U.S. Pacific Northwest [27, 72]. Several long-runout landslide deposits in arid and semiarid regions also contain evidence of the type of substrate liquefaction proposed herein in the form of syn- and postdepositional clastic dikes. Examples from California and Nevada include the Blackhawk, El Capitan, Tin Can Flat, Travertine, and Vallecito landslides [9, 73].

Three field observations support a liquefaction hypothesis for the final movement stages of the ML: (1) the presence of mudflow-like textures exposed along its eroded margin near the mouth of the MSC, (2) the presence of a clastic dike in the northwesterly minor lobe, and (3) the presence of an anomalous sedimentary deposit located immediately northwest of the DH, mapped as unit Qo? on Figure 1.

We attribute the cited evidence of substrate liquefaction to rapid loading and the imposition of major shear stresses on a locally saturated fringe of the alluvial substrate by the rapidly moving landslide debris as it emerged from the

MSC. Based on the estimated depth of scour that occurred below the mountain front, the liquefaction event evidently initiated within the upper 10 m of the original surface just below the mouth of the canyon. We conjecture that this depth coincided with the location of a perched paleo-groundwater table fed by episodic stream flows from the MSC and seepage and springs along the range-bounding frontal fault (expected to act as an aquitard), likely supported by cooler and/or wetter conditions at the time of the landslide circa 100 to 120 ka (Figure 3). We expect that this near surface water lay in a relatively narrow band along the range front, as is commonly the case along range-bounding faults in the Basin and Range province. Given the 27 ha area of the DH and an average thickness of 0.3 m for the liquefied layer, we estimate the process required the entrainment of roughly 80,000 m^3 of saturated alluvium. Given the 300 m width of the debris mass as it exited the main canyon and an excavation depth of 10 m, this would correspond to a width of about 27 m for the wetted zone along the range front. This width correlates well with Google Earth measurements of riparian zone widths along range front faults in areas such as the Wasatch Front, Utah, and the San Andreas Fault Zone of southern California. We envision that, once entrained, the rapid downhill movement of the ML spread the wetted material along the bottom of the debris pile, with agitation keeping it in a liquefied condition for the short duration of runout. Johnson [73] invoked a similar mechanism to explain the exceptional long runout of the Blackhawk landslide of southern California, stating, "…the Blackhawk landslide may have traversed the alluvial apron as a two-layer composite debris flow in which a thick, probably low-fluidity, marble breccia layer rode upon a relatively thin, high-fluidity, sandy mud layer."

Clastic dikes are relatively common in the Blackhawk landslide and several of the other examples listed above. The relative absence of clastic dikes in exposures of the ML may relate to the fact that this landslide occurred in a dryer climate and was smaller, thinner, and lighter than these cited occurrences, thus limiting the amount of liquefied material produced and the overpressures available to inject the fluid into the overlying breccia. Alternatively, liquefied alluvial materials exposed in the bulldozed distal wedge at the cessation of movement may have experienced lateral venting rather than intruding into the overlying breccia to form clastic dikes.

The apparent clastic dike at Location 8 (Figure 1) provides supporting evidence for the presence of shallow groundwater conditions near the mouth of the canyon at the time of the landslide. The material forming the dike appears to consist of fault-related travertine deposits. Based on this evidence, we conjecture that the landslide corresponded in time to a period of active seepage/spring activity at the range-bounding frontal fault and that the landslide incorporated saturated travertine material as it overran the nearby frontal fault.

Potential additional evidence for substrate liquefaction during ML emplacement also occurs far from the mountain front. Wrucke and Corbett [13] mapped the Qo? unit (Figure 1) as a dune deposit. Our geomorphic interpretation

is that this feature may instead represent an outflow of liquefied alluvium that emerged from the toe of the DH upon the cessation of movement. The Qo? deposit has a surface area of about 22 ha and a volume of about 350,000 m³; as such, it would represent about a fifth of the volume of the alluvium we interpret to have scoured by the ML as it descended the alluvial fan. Although a paucity of good field exposures and a mantle of recent alluvium and drift sand complicate its interpretation, the unit is clearly composed largely of alluvial material and not drift sand. Taken together with the flow-like form of the deposit, these sedimentary characteristics provide tentative support for the outflow interpretation.

A potential alternative interpretation of the feature is that it represents a relict alluvial surface dating to the emplacement of the landslide and preserved by the sheltering action of the DH, which tends to deflect upslope runoff toward the floor of the valley. In this interpretation, the flow-like appearance of the deposit in aerial images results from the fortuitous arrangement of erosional channels around the margins of the deposit. Causes of erosion in this area include the lingering effects of landslide-related disturbances to the source watersheds, tectonic, and climatic factors.

Although the debris that would ultimately form the main lobe was moving in excess of 40 m/s when it arrived at the mouth of the MSC, its velocity was still insufficient to convey the debris 1.7 km down the alluvial fan in the absence of some exceptional friction-reducing material or process. The cataclasis model, for example, only predicts another ~500 m of runout below the mountain front (Table 13, Figure 4).

Table 13 provides a detailed summary of the effects of the implied liquefaction event on the runout of the ML as it exited the MSC. This analysis began with the calculated velocities of Blocks 1 through 6 as they exited the mouth of the source canyon (based on application of the cataclasis model, the material represented by Blocks 7 through 9 came to rest in the canyon upstream from the mountain front). Other inputs to the calculation include the slope of the alluvial fan surface and the estimated final locations of the blocks (Table 13; Figure 4, Insert A), which were used as a proxy for the mass distribution, with equal areas assigned to each block. This analysis resulted in the calculation of effective frictional coefficients of 0.13 to 0.16 for the blocks traversing the alluvial fan (Table 13), equivalent to sliding friction angles of approximately 7 to 9 degrees, greatest for the leading edge and lowest for the trailing edge. The higher frictional coefficient of the leading-edge material is attributed to resistance caused by bulldozing of alluvial sediments ahead of the ML during its traverse of the alluvial fan.

Although the calculated coefficients of sliding friction calculated here are rather low, they are nonetheless substantially greater than the inclination of slopes known to experience liquefaction-induced lateral spreads in major seismic events, which can be as low as 1 degree [74]. Residual friction angles of 7 to 9 degrees suggest a residual strength for the liquefied material of about 50 to 60 kPa, consistent with literature values for the upper bound of known incidents of soil liquefaction [75].

In summary, we infer that once the ML debouched onto the alluvial fan at the mouth of the MSC, it liquefied the sub-strate and traversed the fan as essentially a rapid, high strength lateral spread. The overall runout mechanism of the EVL consisted of a hybrid between the cataclasis model in the bedrock canyon areas and liquefaction/lateral spreading on the alluvial fan.

5.7. Alternative Emplacement Mechanisms. Other emplacement mechanisms have been proposed or can be envisioned to explain the long runout and other characteristics of the EVL, of other Blackhawk-like landslides, and of other long-runout landslides in general [2, 8, 10, 16, 17, 20, 27, 29, 47, 49, 55, 72, 73]. We briefly examine the most relevant of these alternate hypotheses here as they relate to the EVL, including (1) sliding on a clay-rich substrate [8], (2) subaqueous emplacement [8], (3) air layer lubrication [10], (4) plastic flow [55], and (5) sliding on a frozen substrate. Proposed mechanical and acoustic grain flow models [2, 47, 49, 54] have already been treated in this discussion and will not be touched upon further here.

5.7.1. Sliding on a Clay-Rich Substrate. Watkins [8] proposed a mechanism for emplacement of the EVL main lobe that invoked basal lubrication by hydrated clay materials. This hypothesis was based on (1) the possible identification of hydrated materials at the base of the landslide in ASTER remote sensing data and (2) the preservation of headscarp stratigraphy and other geologic structures exposed in the deposit.

Watkins [8] utilized remote sensing data collected by the ASTER satellite to evaluate for the presence of clay minerals in the vicinity of the EVL. Table 14 shows the spectral ranges and spatial resolution of the 14 ASTER bands [76]. Watkins [8] cited an ASTER 4 : 8 band ratio image to identify potential hydrated materials (i.e., clays) in the EVL, interpreting a light-colored arc at the toe of the ML in the image to reflect exposures of hydrated clays along the exposed base of the deposit. As reported by Gomez and Lagacherie [77], common clay minerals induce an absorption band around 2200 nm (ASTER band 6), whereas calcium carbonate causes an absorption band around 2340 nm (ASTER band 8; Table 14). Because band 8 reflectance is low for carbonate-rich material, ASTER band 4 : 8 ratio images are not well targeted to the identification of clay minerals but would appear bright for areas rich in carbonates. This conclusion is consistent with the appearance of the ASTER band ratio 4 : 8 image collected in the vicinity of the EVL. Here, slopes underlain by the carbonate-rich upper Wood Canyon, Carrara, and Bonanza King Formations all appear light in tone, whereas slope areas underlain by the Zabriskie Quartzite appear dark, reflecting the relative carbonate content of these formations [31]. Based on these observations, we conclude that the light-colored areas of the ASTER 4 : 8 image cited by Watkins [8] as indicative of areas underlain by hydrated clay minerals, including the light-colored arc at the toe of the ML, in fact highlight areas rich in exposed carbonate materials. We interpret the darker shade of the balance of the ML to reflect its burial by a thin veneer of silica-rich aeolian silt.

While we agree with Watkins [8] that the preservation of headscarp stratigraphy and the structure of the EVL's ML are

TABLE 14: ASTER spectral bands and resolutions [76].

Spectral range	Band no.	Spectral range (nm)	Spatial resolution (m)	Relevant geologic materials [77, 79]
	1	520-600		
Visible-near infrared (Bands 1-3)	2	630-690	15	
	3	780-860		Iron
	4	1600-1700		
	5	2145-2185		
Short wave infrared (Bands 4-9)	6	2185-2225	30	Clays
	7	2235-2285		
	8	2295-2365		Carbonate
	9	2360-2430		
	10	8125-8475		
	11	8475-8825		
Thermal infrared (Bands 10-14)	12	8925-9275	90	
	13	10250-10950		
	14	10950-11650		

consistent with a basal lubrication mechanism, we disagree that clay played any significant role in its runout. Beyond the lack of support for clays in the remote sensing data, our field reconnaissance of the landslide uncovered no visual evidence for clay deposits in the area, and our XRD data (Table 7) demonstrate an almost complete lack of clays in the landslide debris itself. Furthermore, clays do not form reliable lubricants except when saturated and sheared slowly [78]. Based on these observations and considerations, we conclude that clay lubrication is not a viable mechanism for emplacement of the EVL.

5.7.2. Subaqueous Emplacement. Watkins [8] also proposed subaqueous emplacement as a potential alternative (or adjunct) to basal lubrication by hydrated clay materials for the EVL, citing both its long-runout behavior and the morphology of the ML, which "resembles that of some subaqueous landslides." This hypothesis is problematic for a variety of reasons. Subaqueous conditions are, for one, clearly not a necessary precondition for long runout of large, rapid landslides. Moreover, various terrestrial and extraterrestrial landslides share the Blackhawk-like morphology of the EVL, which is also not diagnostic of subaqueous emplacement (Figure 2). Subaqueous emplacement of the EVL is, additionally, problematic because of a lack of evidence for a standing body of water in Eureka Valley during the entirety of the Quaternary period.

Neither lakebed deposits nor geomorphic evidence such as shoreline features exists to support the hypothesis that a standing lake existed in Eureka Valley during Quaternary time [37]. Nearby Owens Valley and Death Valley, by comparison, preserve shoreline features estimated to date from MIS 6 to 12 [80, 81], well older than the estimated maximum age of the EVL. The lack of persistent water bodies in Eureka Valley during the Quaternary period is attributable to its location in the rain shadow of 3000 m to 4000 m high peaks in the Inyo and Sierra Nevada Mountains and to elevated sill heights that preclude inflow from adjacent well-watered watersheds. The most recent persistent lake(s) in the valley date to the mid-Pliocene, approximately 3.5 Ma, likely reflecting paleo-Owens River flow into the valley at that time [37]. Based on the weight of these observations, we consider subaqueous emplacement an unsustainable hypothesis for the EVL.

5.7.3. Air Layer Lubrication Hypothesis. The air layer lubrication hypothesis championed by Shreve [10] to explain the long runout and other peculiarities of the Blackhawk landslide of southern California and its morphological analogs remains a popular hypothesis that often appears in introductory geology texts [82–85]. Objections to the air layer hypothesis for Blackhawk-like landslides include the presence of morphologically similar deposits on nearly airless Mars and truly airless Ceres (Figure 2) as well as a spectrum of other textural and physical issues [17, 73]. Beyond these observations, we include the following specific constraints for the EVL:

(1) *The absence of a mechanism that would allow the landslide debris to reach the mouth of the canyon with sufficient velocity to be launched onto the alluvial fan.* The angle of repose of crushed rock is typically in the range of 35 to 45°, whereas the angle between the source area and the mouth of the MSC is 21°. Hence, barring the action of some mobility-enhancing mechanism from the outset of motion, the landslide debris should not have exited the source canyon at all. Johnson [73] recognized this issue as problematic for the Blackhawk landslide itself.

(2) *The lack of an obvious launch ramp.* The ML traveled down the MSC and debouched onto the alluvial fan at its mouth without encountering an obvious topographic step that would allow it to become airborne to capture and compress a layer of air beneath; and

(3) *Scour of the alluvial substrate accompanying emplacement of the main lobe precludes a "gentle hovercraft-like" descent of the fan by the rapidly moving debris.* The air layer lubrication model envisions the imposition of a compressed air cushion between the alluvial surface and the landslide debris during its traverse of the fan, a concept inconsistent with scour of the alluvial surface by the rapidly moving breccia.

Based on the weight of these observations, we consider air layer lubrication to also represent an unsustainable hypothesis for the EVL.

5.7.4. Plastic Flow. Plastic behavior is a characteristic of many common household substances, such as paint, ketchup, and toothpaste. It has also been proposed to explain the flow of certain materials of geologic origin, including lava flows and debris flows. The fluid-like forms and sheet-like geometries expressed by many long-runout landslides have led to suggestions they too exhibit bulk plastic flow behavior [55]. Such materials experience flow when subjected to basal shear stresses beyond a certain material-dependent "yield stress" [30]. In the case of landslides that exhibit an elevated water content, such behavior is both reasonable and demonstrable [20, 44]. In the case of long-runout landslides composed of dry rock, however, the presence of abrupt internal discontinuities and the preservation of headscarp stratigraphy argue against classical concepts of flow and in favor of basal sliding with localized internal deformation.

Among the diagnostic features of gross plastic behavior is cessation of flow on a slope [30]. It is acknowledged that this attribute is clearly a characteristic of the EVL, which everywhere came to rest on a slope of >3°. Another key attribute of a flowing plastic with a fixed yield strength and density is that its thickness is a direct function of the steepness of the substrate, with steeper slopes producing thinner flows [86]. This condition is clearly violated in the case of the EVL. Equation (19) gives the basic Bingham plastic yield strength formula, which relates these attributes:

$$k = p\, g\, D\, \sin\, \sigma, \tag{19}$$

where k is the Bingham plastic yield strength in Pa, p is the density in kg/m^3, g is the gravitational acceleration in m/s^2, D is the deposit thickness in m, and σ is the ground slope in degrees [30]. Assuming that the k, ρ, and g are constant during landslide emplacement, we can rewrite the preceding equation as follows:

$$D = \text{Constant}/\sin\, \sigma. \tag{20}$$

The significance of Equation (20) is that the larger the slope angle, σ, the smaller the flow thickness, D. To test whether Equation (20) holds for the EVL, we made nine measurements of deposit thickness, D, and ground slope in the movement direction, σ, along the margin of the deposit (Figure 4) using a combination of field measurements and Google Earth topographic profiles along 50 m-long transects parallel to the slide margin. A plot of these data exhibits considerable scatter but generally yields a *positive* correlation between deposit thickness and surface slope (Figure 4, Insert B, dashed line). This trend is the opposite of that anticipated if the landslides were acting as a plastic flow (dotted line in Figure 4, Insert B, calculated assuming a yield strength of 8,500 Pa). Hence, a plastic flow hypothesis is rejected for the EVL because it fails to explain both the details of its interior structure as well as its detailed geometric form.

5.7.5. Sliding on a Frozen Substrate. As shown in Figure 3, the EVL likely occurred during a cooler and possibly wetter-than-present period. As such, we assessed the available evidence for emplacement by sliding on a frozen substrate. Despite the frigid connotations associated with glacial episodes in much of North America, Eureka Valley lies far to the south of the recognized southern limit of permanently frozen ground in North America during the last glacial maximum (MIS 2) [87]. Moreover, peak temperatures in Death Valley generally stood about 10°C higher during the time assigned to the landslide than during the last glacial maximum (Figure 3), further reducing the likelihood of emplacement on an ice-covered surface or buried permafrost layer. The inferred 10 m deep excavation of the alluvial substrate during emplacement of the ML also precludes sliding on a temporary surficial sheet of ice or mantle of snow following a rare freeze or snowstorm. Hence, we consider sliding on a frozen substrate an improbable mechanism for emplacement of the ML.

6. Conclusions

Between approximately 60 and 120 ka, a block of Cambrian-age limestone with a volume exceeding 5 million m^3 detached along a planar discontinuity at its source in the Last Chance Range and rapidly accelerated downhill. The moving mass of breccia separated into two unequal lobes at the base of its initial plunge. The smaller lobe, comprising roughly 40% of the failed mass, traveled to the south and came to rest in a side canyon. The larger lobe passed to the north of the ridge and traveled the full length of the main source canyon, with most of its mass ultimately debouching onto the alluvial fan at its mouth. Upon reaching the mouth of the MSC, the main lobe excavated a ~10 m deep trench down the length of the alluvial fan and incorporated about 1.6 million m^3 of displaced material into its mass, thickening and widening its distal heap.

Pervasive brecciation of the slidemass accompanied detachment of the slidemass from the mountainside and its transit through the bedrock canyon areas. Rather than being a simple by-product of the landslide process, we interpret slidemass brecciation to instead reflect a key process underlying the movement of large, rapid landslides that traverse rocky slopes and canyons. The physical process envisioned here involves recycling of the elastic energy of the breaking clasts into the moving debris, greatly enhancing landslide mobility. This process, in principle, should function in any terrestrial or extraterrestrial setting in which the constituent rock mass can experience brittle, impact-driven tensile, or shear failure during emplacement.

As the ML exited the MSC, it encountered a much weaker, locally wet, alluvial substrate that succumbed to liquefaction in response to rapid loading and shearing, prompting a second phase of movement. Taking over from the cataclasis-driven mechanism as the debris exited the MSC, basal liquefaction extended the reach of the rapidly moving debris by roughly a kilometer beyond that possible by way of the cataclasis mechanism alone.

No field evidence exists to support alternative mechanisms such as sliding on a basal layer of saturated clay, frozen ground, or air. The field evidence also excludes subaqueous emplacement of the ML, emplacement as a plastic flow, or mobilization of the landslide by any mechanism requiring the constituent clasts to maintain their integrity (such as acoustic or mechanical grain flow).

These findings present a means to better predict the reach of future long-runout landslides that often accompany large-scale slope failures. Among the key insights provided by this research is the recognition that the dimensions of the failed source block, the geometry of the runout track, and the nature of the substrate all play significant roles in governing the runout experienced by large, rapid slope failures, and thus, all represent important elements in assessing the risks afforded by future large-scale mass movements. In the face of the extremely violent and energetic forces applied by a large, rapid landslide on its base, the behavior of the weakest material prevails. When traveling over a rock surface, it is the strength of the constituent clasts that govern the process, but when the debris encounters a weak substrate, such as a saturated soil, the properties of the soil govern.

The consequential geologic, geometric, and environmental factors addressed herein should, in most instances, be accessible and quantifiable by qualified field personnel. In areas of extreme sensitivity, such as rugged watersheds hosting (or lying upstream from) large population centers, such investigations seem warranted. A key to exploiting this opportunity is the successful hindcast of other well-constrained long-runout landslides in the historical and geologic record.

Data Availability

Data supporting conclusions reported in this study consist of maps cited within the manuscript as well as field photos, that will be provided in pdf format from the principal author upon request.

Conflicts of Interest

The authors declare that there is no conflict of interest regarding the publication of this article.

Acknowledgments

References

[1] D. M. Cruden and J. Krahn, "Frank rockslide, Alberta, Canada," in *Rockslides and Avalanches, 1, Natural Phenomena*, B. Voight, Ed., pp. 97–112, Elsevier Scientific Publishing Co., New York, New York, 1978.

[2] K. J. Hsü, "Catastrophic debris streams (sturzstroms) generated by rockfalls," *Geological Society America Bulletin*, vol. 86, no. 1, pp. 129–140, 1975.

[3] G. Plafker and G. E. Ericksen, "Nevados Huascaran avalanches, Peru," in *Rockslides and Avalanches, 1, Natural Phenomena*, B. Voight, Ed., pp. 277–314, Elsevier Scientific Publishing Co., New York, New York, 1978.

[4] ASDSO, *Vaiont Dam (Italy, 1963): lessons learned from dam incidents and failures*, 2019, September 2019, https://damfailures.org/case-study/vajont-dam-italy-1963/.

[5] J. E. Costa and R. L. Shuster, "The formation and failure of natural dams," *Geological Society of America Bulletin*, vol. 100, no. 7, pp. 1054–1068, 1988.

[6] Food and Agriculture Organization of the United Nations (FAO), *The Aral Sea transboundary river basin*, 2012, September 2019, http://www.fao.org/nr/water/aquastat/basins/aral-sea/aral.sea-CP_eng.pdf.

[7] J. S. McKeown and K. M. Bishop, "The Eureka Valley landslide – a two-lobed deposit from a single event in the Last Chance Range of Death Valley," *CA: AEG Annual Meeting Program Abstracts*, vol. 52, p. 90, 2009.

[8] J. A. Watkins, *Tectonic and aqueous processes in the formation of mass-wasting features on Mars and Earth*, [Ph.D. thesis]: Los Angeles, University of California, Los Angeles, 2015.

[9] P. J. Shaller, *Analysis and implications of large martian and terrestrial landslides*, [Ph.D. thesis]: California Institute of Technology, Pasadena, 1991.

[10] R. L. Shreve, "The Blackhawk Landslide," *Geological Society America Special Paper*, vol. 108, p. 47, 1968.

[11] T. C. Blair, "Alluvial fan and catchment initiation by rock avalanching, Owens Valley, California," *Geomorphology*, vol. 28, no. 3-4, pp. 201–221, 1999.

[12] L. Fauque and M. R. Strecker, "Large rock avalanche deposits (Sturzstrome, sturzstroms) at Sierra Aconquija, northern Sierras Pameanas, Argentina," *Eclogae Geologicae Helvetiae*, vol. 81, pp. 579–592, 1988.

[13] C. T. Wrucke and K. P. Corbett, *Geologic map of the Last Chance quadrangle, California and Nevada: United States Geological Survey, Open-File Report Map 90-647A, scale 1: 62 500, 1 sheet*, 1990.

[14] T. M. Schlom and J. R. Knott, "Earthquake magnitude and recurrence from scarp morphology, Eureka Valley fault zone, eastern California," *Geological Society America Abstracts with Programs*, vol. 41, no. 7, p. 670, 2009.

[15] K. H. G. Hughson, *Personnel Communication*, 2017.

[16] A. Heim, *Bergsturz und Menschenleben: Zurich, Switzerland, Fretz & Wasmuth Verlag A. G*, BiTech Publishers, Vancouver, British Columbia, Canada, 1932.

[17] P. J. Shaller and A. Shaller, "Review of proposed mechanisms of sturzstroms (long-runout landslides)," in *Sturzstroms and detachment faults, Anza-Borrego State Park*, P. L. Abbott and D. C. Seymour, Eds., pp. 185–202, South Coast Geological

Society, Annual Field Trip Guidebook No. 24, California, 1996.

[18] D. E. French and P. L. Guth, *Megabreccias of the Sheep Range*, Nevada Petroleum & Geothermal Society, 2016 Field Trip, Clark County, Nevada, 2016.

[19] J. Walker and D. E. French, *Prolific megabreccia reservoir in Railroad Valley, Nye County, Nevada: key to future discoveries: AAPG Rocky Mountain Section Annual Meeting*, 2017.

[20] P. J. Shaller, "Analysis of a large moist landslide, Lost River range, Idaho, U.S.A," *Canadian Geotechnical Journal*, vol. 28, no. 4, pp. 584–600, 1991.

[21] E. Nunez Jr., J. R. Knott, A. Zepeda, and T. M. Schlom, *Fault scarp morphology along the Eureka Valley fault zone*, vol. 45, no. 6, 2013, Geological Society America, Abstracts with Programs, Eastern California, U.S.A, 2013.

[22] G. Peltzer, P. Rosen, F. Rogez, C. Werner, E. Fieldings, and K. Hudnut, "Crustal deformation studies using synthetic aperture radar (SAR) interferometry," in *FRINGE 96 Workshop: ERS SAR Interferometry, Zurich, 30 September – 2 October 1996*, European Space Agency Publications Division, SP-406, Noordwijk, The Netherlands, 1996.

[23] US Geological Survey, *Quaternary Faults & Folds in the U.S.: USGS Earthquake Hazards Program, Google Earth/KML Files*, 2019, June 2020, https://earthquake.usgs.gov/learn/kml.php.

[24] S. E. Hough and K. Hutton, "Revisiting the 1872 Owens Valley, California," *Earthquake: Bulletin of the Seismological Society of America*, vol. 98, no. 2, pp. 931–949, 2008.

[25] J. R. Knott, A. M. Sarna-Wojcicki, M. N. Machette, and R. E. Klinger, "Upper Neogene stratigraphy and tectonics of Death Valley - a review," *Earth-Science Reviews Special Issue*, vol. 73, no. 1-4, pp. 245–270, 2005.

[26] W. B. Bull, "The alluvial fan environment," *Progress in Physical Geography*, vol. 1, pp. 222–270, 2016.

[27] O. Hungr and S. G. Evans, "Entrainment of debris in rock avalanches," *An analysis of a long-runout mechanism: GSA Bulletin*, vol. 116, pp. 1240–1252, 2004.

[28] C. R. Longwell, "Megabreccia developed downslope from large faults [Arizona-Nevada]," *American Journal Science*, vol. 249, no. 5, pp. 343–355, 1951.

[29] C. G. Bock, "The Martinez Mountain rock avalanche," in *Landslides*, D. R. Coates, Ed., vol. 3, pp. 155–168, Geological Society of America Reviews in Engineering Geology, 1977.

[30] A. M. Johnson, *Physical Processes in Geology: San Francisco*, California, Freeman, Cooper & Co, 1970.

[31] National Park Service, *Geologic formations*, Death Valley, California, 2015, March 2019, http://www.nps.gov/deva/naturescience/geologicformations.htm.

[32] J. P. McCalpin and E. W. Hart, *Ridgetop spreading features and relationship to earthquakes, San Gabriel Mountains region, southern California – part A: distribution and description of ridgetop depressions (sackungen): Final Technical Report Contract 1434-HQ-GR-1026, National Earthquake Hazards Reduction Program*, Geological Survey, U.S, 2002.

[33] Western Regional Climate Centerhttps://wrcc.dri.edu/cgi-bin/rawMAIN.pl?caCEUR.

[34] M. L. Stout, "Radiocarbon dating of landslides in southern California," *California Geology*, vol. 30, no. 5, pp. 99–105, 1977.

[35] Y. Matsubara and A. D. Howard, "A spatially explicit model of runoff, evaporation, and lake extent: Application to modern and late Pleistocene lakes in the Great Basin region, western

[36] J. Knott, *Personal communication*, 2019.

[37] J. R. Knott, E. Wan, A. L. Deino et al., "Lake Andrei: A pliocene pluvial lake in Eureka Valley, eastern California," in *From Saline to Freshwater: The Diversity of Western Lakes in Space and Time*, S. Starratt and M. R. Rosen, Eds., vol. 536, pp. 125–142, Geological Society of America Special Paper, 2019.

[38] T. K. Lowenstein, J. Li, C. Brown et al., "200 k.y. paleoclimate record from Death Valley salt core," *Geology*, vol. 27, no. 1, pp. 3–6, 1999.

[39] University of Georgia, *Marine isotope stages and substages, Railsback's Some Fundamentals of Mineralogy and Geochemistry*, 2015, October 2019, http://www.gly.uga.edu/railsback/Fundamentals/SFMGSubstages01.pdf.

[40] J. Singh, *Dictionary of Physics*, Stirling Publishers Pvt Ltd., New Delhi, 2007.

[41] E. Scheller, "Beitrag zum Bewegungsverhalten grosser Bergstürze," *Eclogae Geologicae Helvetiae*, vol. 64, pp. 195–202, 1971.

[42] B. K. Lucchitta, "A large landslide on Mars," *Geological Society America Bulletin*, vol. 89, no. 11, pp. 1601–1609, 1978.

[43] A. J. L. Harris, L. P. Flynn, O. Matias, W. I. Rose, and J. Cornejo, "The evolution of an active silicic lava flow field: an ETM+ perspective," *Journal Volcanology Geothermal Research*, vol. 135, no. 1-2, pp. 147–168, 2004.

[44] P. J. Shaller, P. L. Shrestha, M. Doroudian, D. W. Sykora, and D. L. Hamilton, "Numerical modeling of the 2005 La Conchita landslide, Ventura County, CaliforniaFlood Hazard Identification and Mitigation in Semi- and Arid Environments," World Scientific, New Jersey, 2012.

[45] T. De Haas and T. Van Woerkom, "Bed scour by debris flows: experimental investigation of effects of debris-flow composition," *Earth Surface Processes Landforms*, vol. 41, no. 13, pp. 1951–1966, 2016.

[46] R. M. Iverson, "The physics of debris flows," *Reviews of Geophysics*, vol. 35, no. 3, pp. 245–296, 1997.

[47] H. J. Melosh, "Acoustic fluidization," *American Scientist*, vol. 71, pp. 158–165, 1983.

[48] P. K. Haff, "Grain flow as a fluid-mechanical phenomenon," *Journal Fluid Mechanics*, vol. 134, pp. 401–430, 1983.

[49] C. S. Campbell, P. W. Cleary, and M. Hopkins, "Large-scale landslide simulations: Global deformation, velocities and basal friction:," *Journal Geophysical Research Solid Earth*, vol. 100, no. B5, pp. 8045–8499, 1995.

[50] P. J. Shaller, E. L. Mathieson, and S. Okubo, *The Travertine rock avalanche, southern Santa Rosa Mountains, southeastern California*, vol. 52, AEG Annual Meeting Program Abstracts, Lake Tahoe, CA, 2009.

[51] G. Shanmugam, *Handbook of Petroleum Exploration and Production*, Turbidity current, 2012, June 2020, https://www.sciencedirect.com/topics/earth-and-planetary-sciences/turbidity-current.

[52] R. V. Fisher, *Deposits of pyroclastic sediment gravity flows*, 1997, June 2020, http://volcanology.geol.ucsb.edu/deposits.htm.

[53] T. Bourbie, O. Coussy, and B. Zinszner, *Acoustics of Porous Media*, CRC Press, United States, 1st edition, 1988.

[54] C. S. Campbell, "Granular material flows – an overview," *Powder Technology*, vol. 162, no. 3, pp. 208–229, 2006.

United States," *Water Resources Research*, vol. 45, no. 6, article W06425, 2009.

[55] A. S. McEwen, "Mobility of large rock avalanches," *Evidence from Valles Marineris, Mars: Geology*, vol. 17, pp. 1111–1114, 1989.

[56] A. Refahi, J. A. Mohandesi, and B. Rezai, "Comparison between bond crushing energy and fracture energy of rocks in a jaw crusher using numerical simulation," *Journal Southern African Institute Mining Metallurgy*, vol. 109, pp. 709–717, 2009.

[57] D. Legendre and R. Zevenhoven, "Assessing the energy efficiency of a jaw crusher," *Energy*, vol. 74, pp. 119–130, 2014.

[58] A. Afrouz, *Practical Handbook of Rock Mass Classification Systems and Modes of Ground Failure*, CRC Press, Ann Arbor, MI, 1992.

[59] N. R. Barton, *A review of the shear strength of filled discontinuities in rock*, vol. 105, Norwegian Geotechnical Institute, Publication No, Oslo, Norway, 1974.

[60] R. L. Stowe, *Strength and Deformation Properties of Granite, Basalt, Limestone and Tuff at Various Loading Rates*, Army Corps of Engineers Waterways Experiment Station, Miscellaneous Paper C-69-1, U.S, 1969.

[61] C. Young and O. Dubugnon, "A reflected shear-wave technique for determining dynamic rock strength," *International Journal of Rock Mechanics and Mining Sciences & Geomechanics Abstracts*, vol. 14, no. 5–6, pp. 247–259, 1977.

[62] Y. V. Petrov, I. V. Smirnov, G. A. Volkov, A. K. Abramian, A. M. Bragov, and S. N. Verichev, "Dynamic failure of dry and fully saturated limestone samples based on incubation time concept," *Journal of Rock Mechanics and Geotechnical Engineering*, vol. 9, no. 1, pp. 125–134, 2017.

[63] B. C. Haimson, "Effect of cyclic loading on rock," in *Dynamic Geotechnical Testing*, M. Silver and D. Tiedemann, Eds., pp. 228–245, ASTM International, West Conshohocken, Pennsylvania, 1978.

[64] T. Okada and T. Naya, "A new model for evaluating the dynamic shear strength of rocks based on laboratory test data for earthquake-resistant design," *Journal of Rock Mechanics and Geotechnical Engineering*, vol. 11, no. 5, pp. 979–989, 2019.

[65] F. Zou, Z. Fang, and M. Xia, "Study on dynamic mechanical properties of limestone under uniaxial impact compressive loads," *Mathematical Problems in Engineering*, vol. 2016, Article ID 5207457, 11 pages, 2016.

[66] ASTM D3967-16, *Standard test method for splitting tensile strength of intact rock core specimens*https://www.astm.org/Standards/D3967.

[67] E. T. Selig and D. L. Boucher, "Abrasion tests for railroad ballast," *Geotechnical Testing Journal*, vol. 13, no. 4, pp. 301–311, 1999.

[68] B. R. Watters, M. J. Klassen, and A. W. Clifton, "Evaluation of ballast materials using petrographic criteria," in *Transportation Research Record 1131, Performance of Aggregates in Railroads and Other Track Performance Issues*, pp. 45–63, Transportation Research Board, Wahington D.C., 1987.

[69] B. Cerfontaine and F. Collin, "Cyclic and fatigue behaviour of rock materials," *Review, interpretation and research perspectives: Rock Mechanics and Rock Engineering*, vol. 51, no. 2, pp. 391–414, 2018.

[70] T. Kamonphet, S. Khamrat, and K. Fuenkajorn, "Effects of cyclic shear loads on strength, stiffness and dilation of rock fractures," *Songlanakarin Journal of Science and Technology*, vol. 37, no. 6, pp. 683–690, 2015.

[71] E. C. Surinach, I. Vilajosana Guillén, G. Khazaradze, B. Biescas Górriz, G. Furdada Bellavista, and J. M. Vilaplana, "Seismic detection and characterization of landslides and other mass movements," *Natural Hazards and Earth System Sciences*, vol. 5, pp. 761–798, 2005.

[72] B. D. Collins and M. E. Reid, "Enhanced landslide mobility by basal liquefaction: the 2014 state route 530 (Oso), Washington, landslide," *Geological Society of America Bulletin*, vol. 134, no. 3-4, pp. 451–476, 2019.

[73] B. Johnson, "Blackhawk landslide, California, U.S.A.," in *Rockslides and Avalanches 1, Natural Phenomena*, B. Voight, Ed., pp. 481–504, Elsevier, New York, New York, 1978.

[74] T. L. Youd, "Liquefaction-induced lateral ground displacement," in *International Conferences on Recent Advances in Geotechnical Earthquake Engineering and Soil Dynamics, 3*, pp. 911–925, St. Louis, Missouri, 1995.

[75] I. M. Idriss and R. W. Boulanger, *Soil Liquefaction during Earthquakes*, Earthquake Engineering Research Institute, Oakland, CA, 2008.

[76] Satellite Imaging Corporation, *ASTER Satellite Sensor*, 2017, October 2019, https://www.satimagingcorp.com/satellite-sensors/other-satellite-sensors/aster/.

[77] C. Gomez and P. Lagacherie, "Mapping of primary soil properties using optical visible and near infrared (Vis-NIR) remote sensing," in *Land Surface Remote Sensing in Agriculture and Forest*, N. Baghdadi and M. Zribi, Eds., pp. 1–35, Elsevier, 2016.

[78] P. J. Shaller, "Long-runout landslides and the long-lasting effects of early water activity on Mars: COMMENT," *Geology*, vol. 44, no. 5, p. 386, 2016.

[79] M. Massironi, L. Bertoldi, P. Calafa et al., "Interpretation and processing of ASTER data for geological mapping and granitoids detection in the Saghro massif (eastern Anti-Atlas, Morocco)," *Geosphere*, vol. 4, no. 4, pp. 736–759, 2008.

[80] A. S. Jayko and S. N. Bacon, "Late Quaternary MIS 6–8 shoreline features of pluvial Owens Lake, Owens Valley, eastern California," in *Late Cenozoic Drainage History of the Southwestern Great Basin and Lower Colorado River Region: Geologic and Biotic Perspectives*, M. C. Reheis, R. Hershler, and D. M. Miller, Eds., pp. 185–206, Geological Society of America Special Paper 439, 2008.

[81] L. A. Owen, K. L. Frankel, J. R. Knott et al., "Beryllium-10 terrestrial cosmogenic nuclide surface exposure dating of Quaternary landforms in Death Valley," *Geomorphology*, vol. 125, no. 4, pp. 541–557, 2011.

[82] S. Marshak, *Essentials of Geology*, W.W. Norton & Co., New York, 5th edition, 2016.

[83] D. Nance and B. Murphy, *Physical Geology Today*, Oxford University Press, New York, 2016.

[84] C. C. Plummer, D. H. Carlson, and L. Hammersley, *Physical Geology*, McGraw-Hill Education, New York, 15th edition, 2016.

[85] E. J. Tarbuck and F. K. Lutgens, *Earth: An Introduction to Physical Geology*, Pearson, New York, 12th edition, 2017.

[86] A. M. Johnson, "Debris flow," in *Slope Instability*, D. Brunsden and D. B. Prior, Eds., pp. 257–361, John Wiley & Sons, New York, 1984.

[87] R. J. E. Brown and T. L. Péwé, "Distribution of permafrost in North America and its relationship to the environment: a review," in *Permafrost: North American contribution [to the] Second International Conference, Yakutsk, Siberia, USSR*, pp. 71–100, National Academy of Sciences, Washington D.C., 1973.

Supplemental Figures

Figure S1. Detailed Site Location Map, modified from Caltrans http://www.dot.ca.gov/d9/maps/index.html

Figure S2. Feature 2: View to east of large talus accumulation in the headscarp bowl, 37.068° N, 117.620° W.

Figure S3. Feature 3: Playa sediments at the head of the PML at 37.068° N, 117.628° W.

Figure S4. Feature 4: Erosional arch in landslide breccia near the head of the PML at 37.068° N, 117.630° W.

Figure S5. Feature 5: Playa located near the head of the distal heap at 37.074° N, 117.648° W.

Figure S6. Feature 6: Exposure of alluvial material at the margin of the possible outflow lobe at 37.080° N, 117.651° W. Measuring staff subdivisions at 1 inch and 6 inches. Dark red surface clasts derived from Dedeckera Canyon watershed.

Figure S7. Feature 7: Exposure of range-bounding frontal fault and associated travertine deposits at 37.078° N, 117.640° W.

Figure S8. Feature 8: Exposure of northwestern side lobe (on skyline, indicated by arrows) in northerly side canyon at 37.075° N, 117.636° W.

Figure S9. Feature 9: Exposure of northern side lobe composed of yellow-brown Carrara limestone draped over brown Wood Canyon bedrock at 37.075° N, 117.633° W.

Figure S10. Feature 10: Isolated remnants of Carrara Formation (yellow-orange) breccoa mantling slopes of main source canyon at 37.072° N, 117.631° W.

Figure S11. Detailed view of a fine-grained sample of clast-supported angular to sub-rounded breccia in the main lobe.
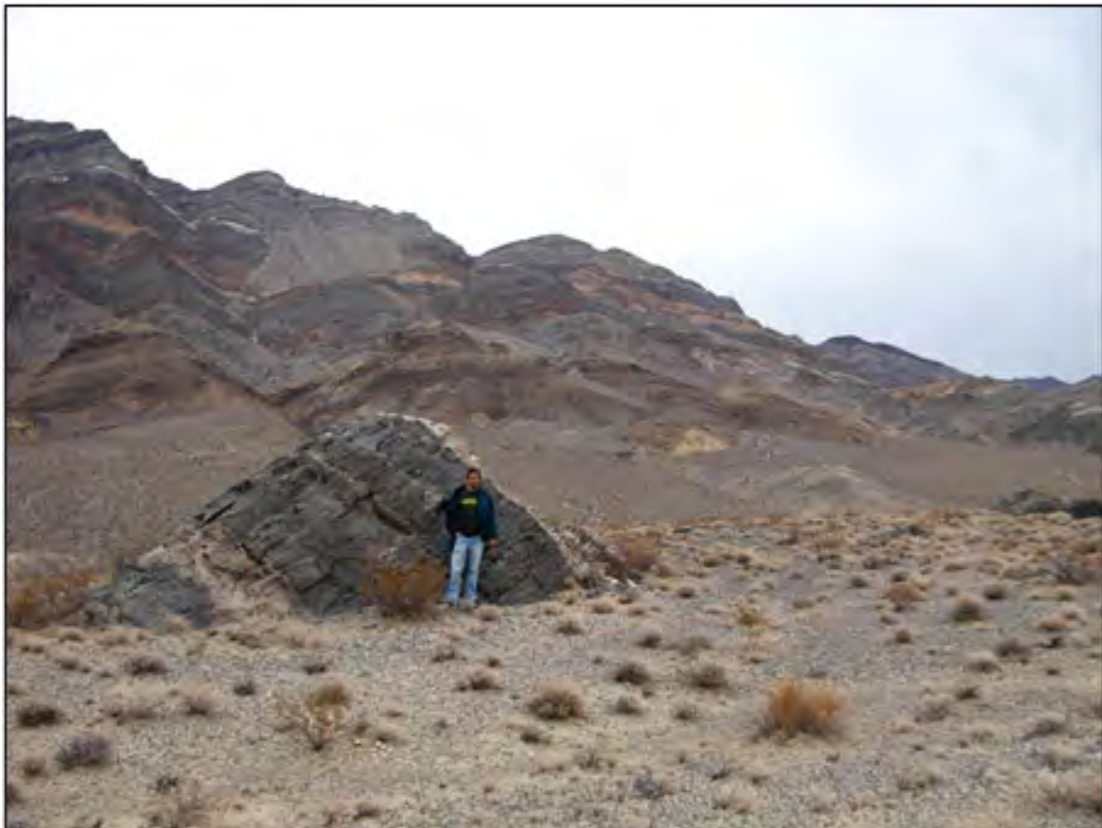
Figure S12. Large, rafted block of Bonanza King Formation limestone capping the distal heap at 37.076° N, 117.651° W.
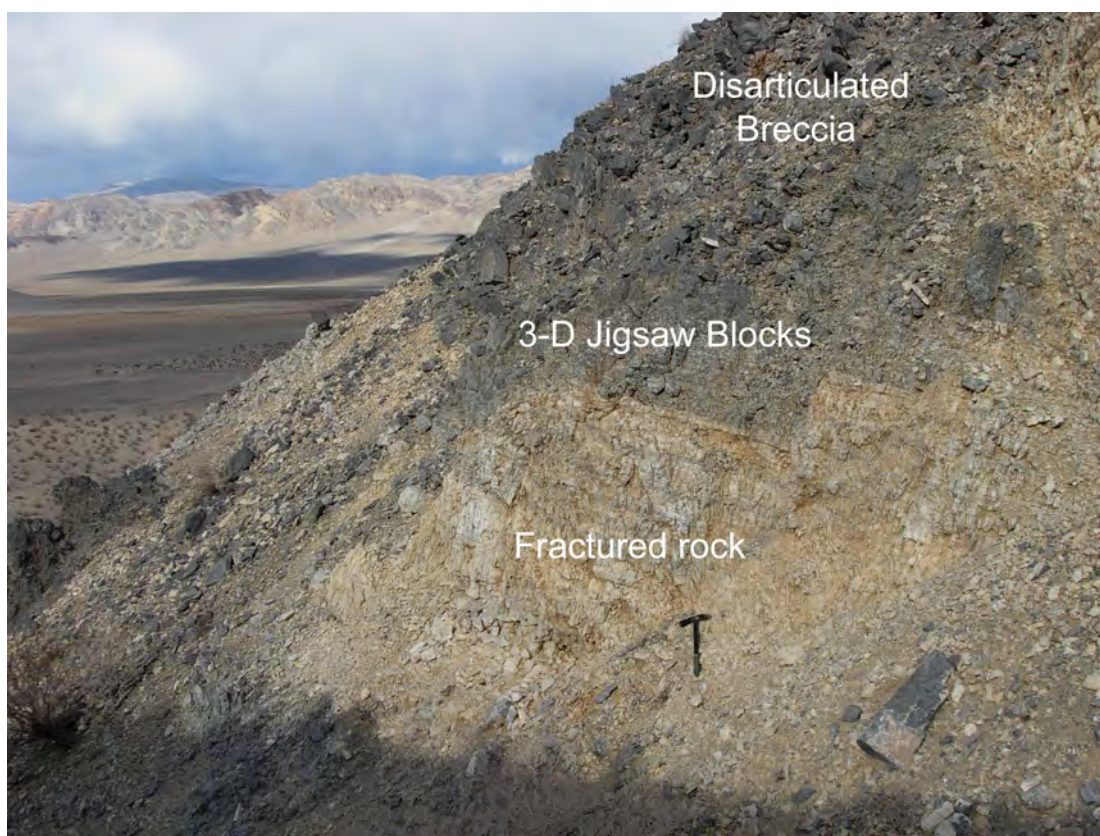
Figure S13. Detail view of landslide breccia near toe of main lobe. Texture grades from fractured but largely intact rock to disarticulated breccia. The intervening mass represents "three dimensional jigsaw puzzle block" texture described from other long-runout landslides. Note geologist's pick in lower center for scale.

Figure S14. Exposure of interior of main lobe, showing abrupt color and textural changes across a narrow shear plane (dashed line) and contorted texture below.

Figure S15. Reverse fault feature (dashed, with opposing arrows) with associated minor faults and drag folds exposed along northern edge of the distal heap at 37.076° N, 117.648° W.
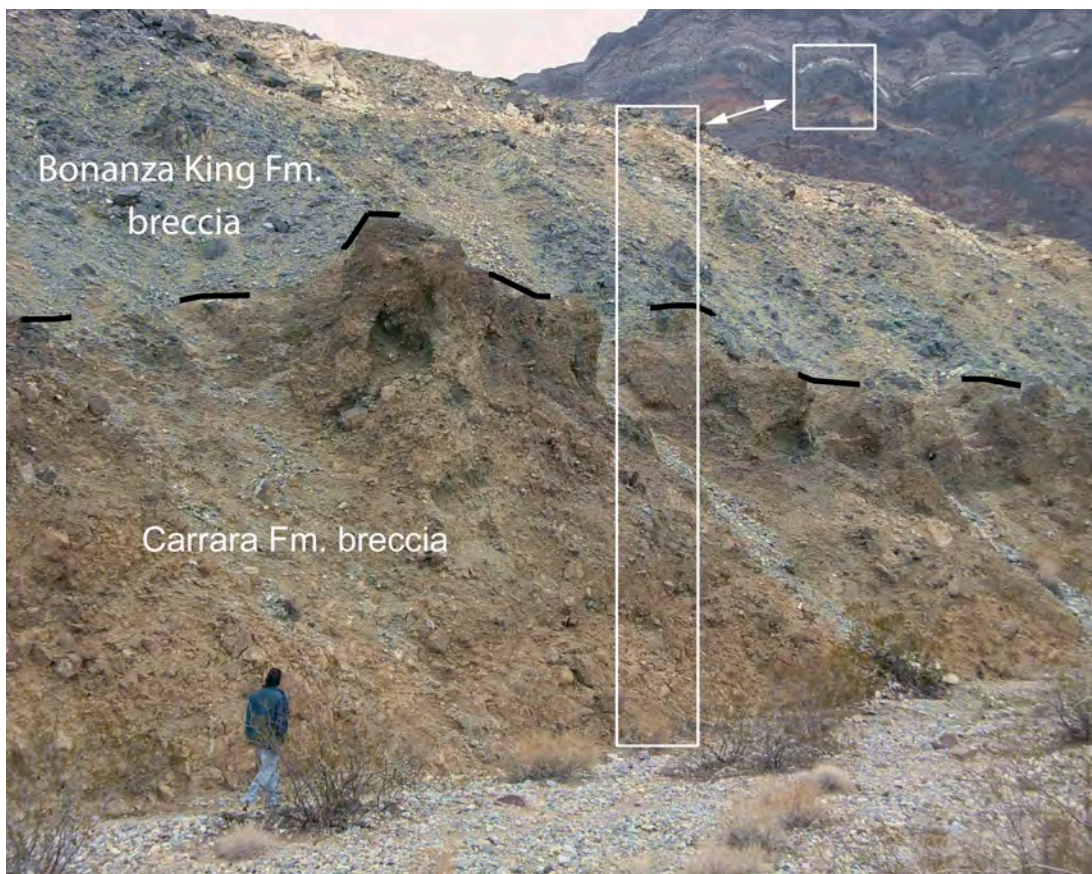
Figure S16. Preservation of attenuated headscarp stratigraphy on the south flank of the main lobe. Correlative source area and deposit stratigraphy indicated by white boxes.
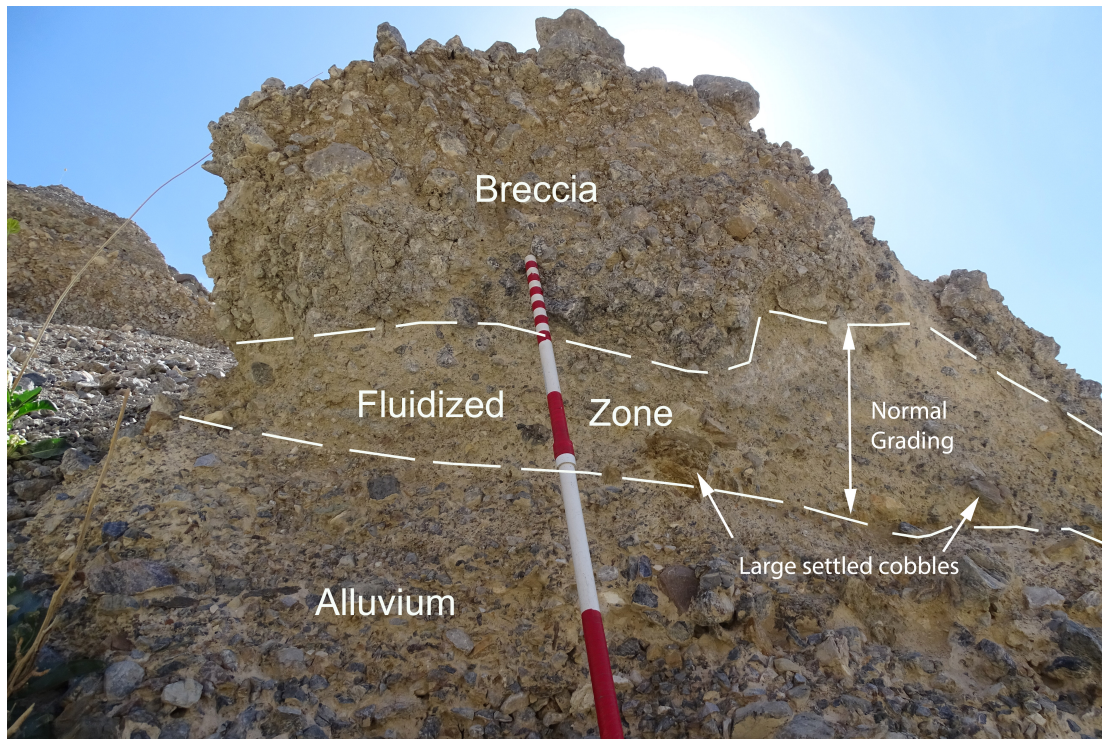
Figure S17. View to southwest along eroded northern margin of the main lobe, showing geologic interpretation of the exposed materials. Measuring staff delineations at 1 foot, 6 inches, and 1 inch.

Figure S18. Chevron fold composed of light-colored breccia exposed in PML near 37.068° N, 117.632° W.
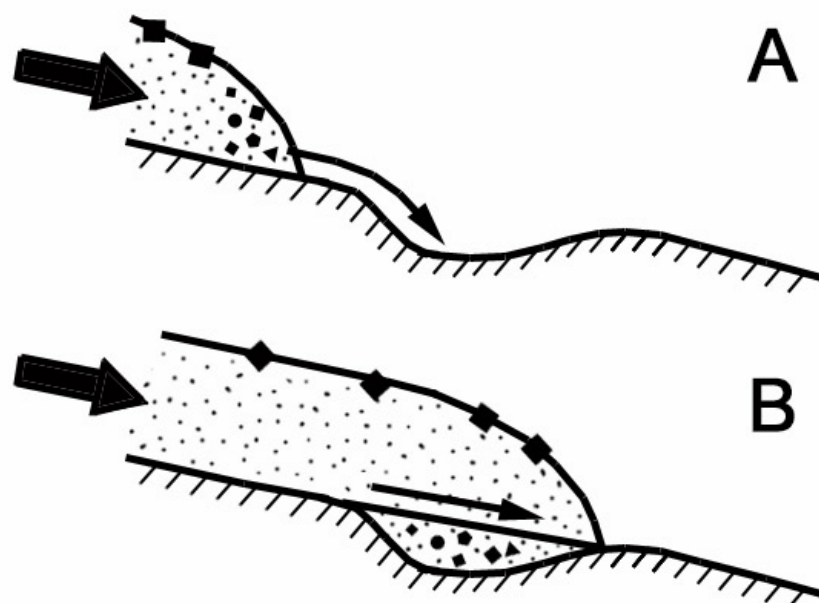
Figure S19. Schematic diagram showing interpreted pattern of deposition from leading edge of the landslide during runout. Coarser clasts concentrated at the leading edge of the landslide (indicated by larger symbols) are deposited in depressions in the travel path during runout (A), simplifying the runout geometry of finer trailing material (B).

Figure S20. Exposure of base of PML showing fine breccia overlying coarse-grained breccia at base of slide.

Figure S21. Crest of northern minor lobe showing pervasively fractured Carrara and Bonanza King Formation blocks in preserved stratigraphic sequence. Note pervasive cavernous weathering of exposed blocks.

Figure S22. Base of northerly minor lobe, showing substantial admixture of brown Wood Canyon clasts.

Figure S23. Basal exposure of northerly minor lobe, showing Carrara Formation breccia in contact with Wood Canyon Formation bedrock. Note pale color and fluid character of matrix at contact.

Figure S24. Clastic dike composed of white sandy gravel injected into block of Bonanza King limestone, about 10 vertical meters above the contact shown in preceding image.

Figure S25. South proximal margin of the main lobe at the mouth of the main source canyon near 37.070° N, 117.638° W. Arrows point at the outside edge of the deposit.
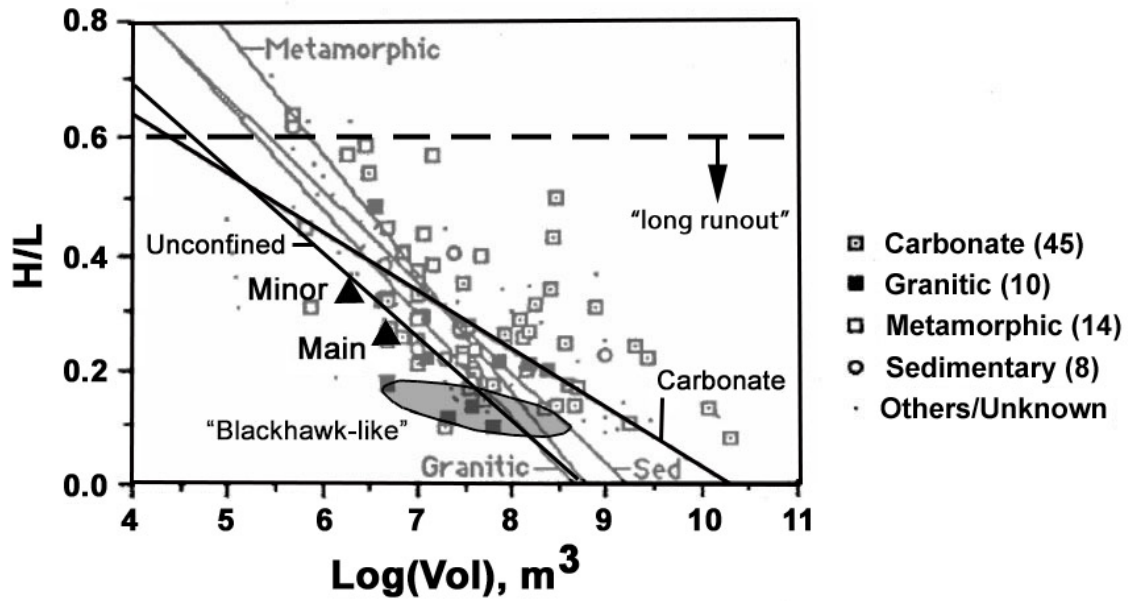
Figure S26. Log(Volume, bulked) vs. H/L plots for 90 terrestrial subaerial nonvolcanic long-runout landslides, modified from Shaller [9], showing data for the main and principal minor lobes of the Eureka Valley landslide. Various lithology-specific data points and their assicated regression lines are shown, with the number of deposits in each group indicated in legend at right. Also highlighted are the regression lines for carbonate and unconfined landslides and the small region of the chart occupied by "Blackhawk like" landslides.
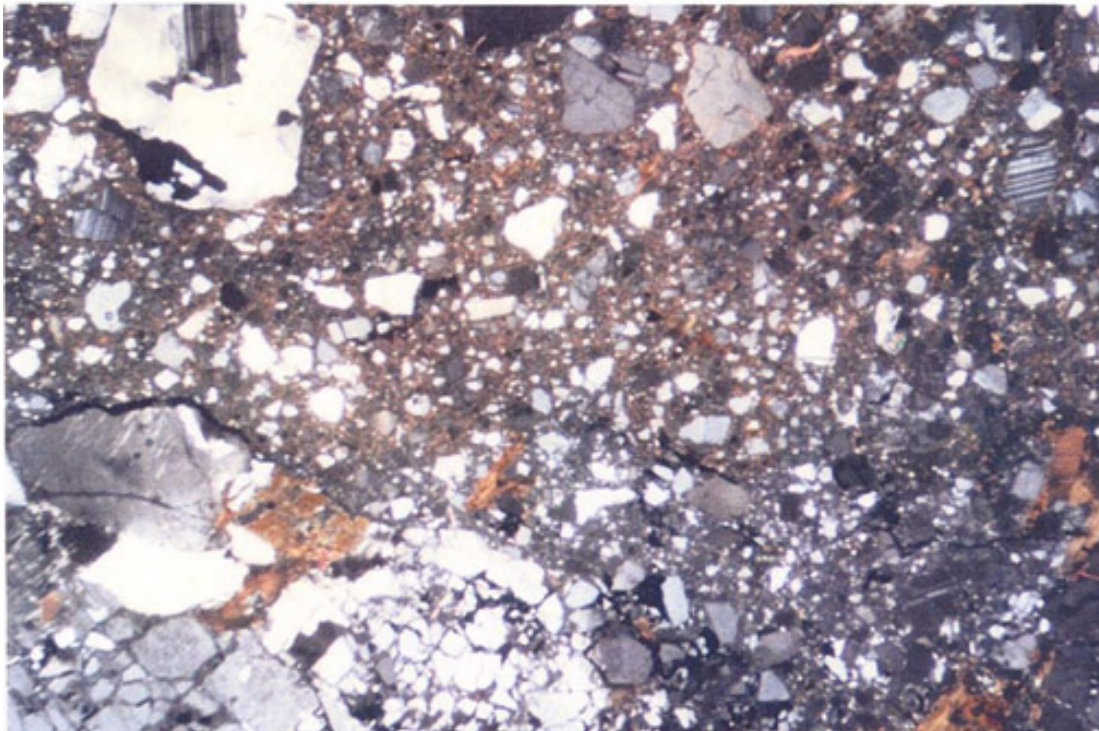

Figure S27. Polarized light thin section of granodiorite microbreccia from the base of the Martinez Mountain landslide, California [9]. Note mixture of pervasively fractured grains and independent mineral grains in fine matrix.
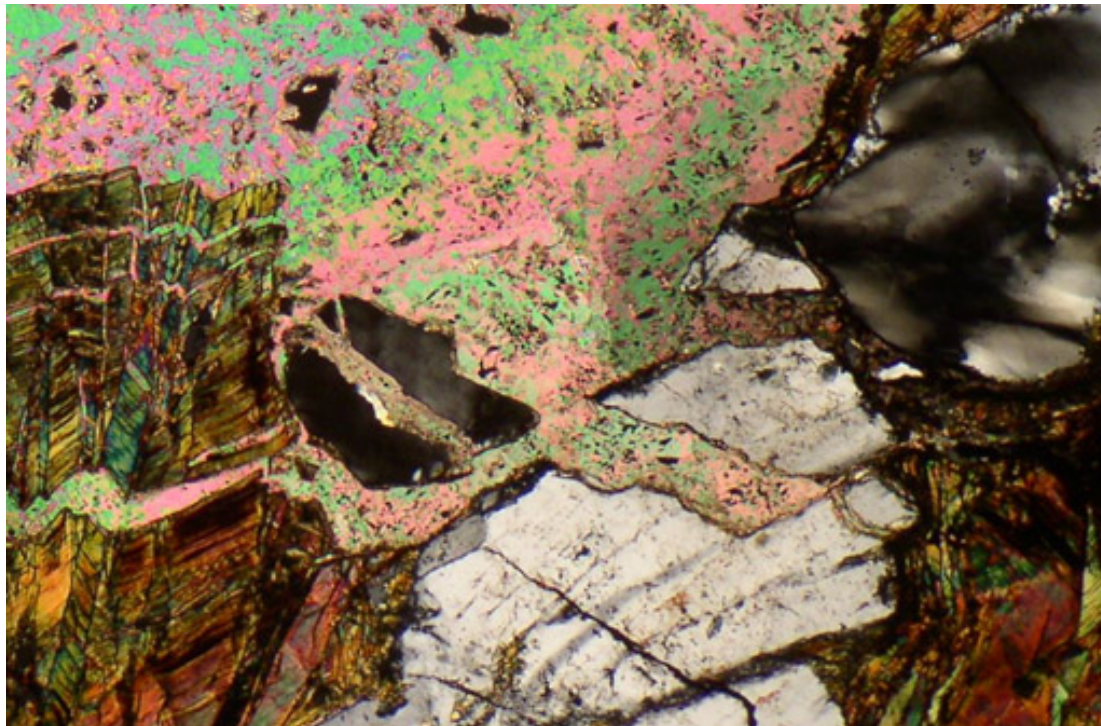
Figure S28. Polarized light thin section of granodiorite breccia from the base of the Travertine landslide, California [50]. Note separation of matching crystal fragments separated by intrusion of pale carbonate matrix.
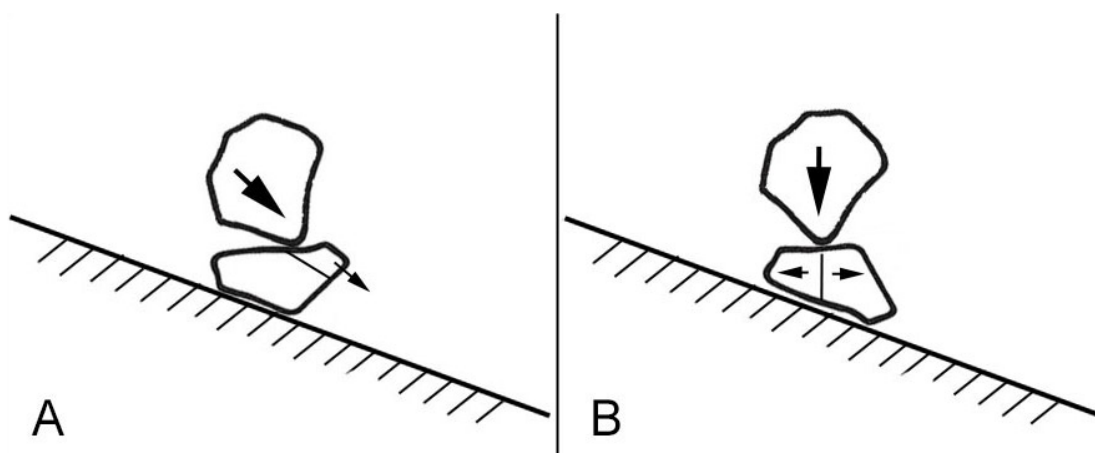

Figure 29S. Anticipated impact failure modes for clasts entrained in the Eureka Valley landslide: A) Shear failure of a target clast experiencing a glancing blow from a fellow clast moving at a high relative velocity; B0 Tensile failure of a target clast after experiencing a normally-drected blow from a fellow clast moving at a high relative velocity.